15 Feb 2023

Simulation of Natural Tornado Genesis and Evolution from an Initial Instability Profile

Kakkattukuzhy M. Issac
Missouri University of Science and Technology, isaac@mst.edu

Simulation of Natural Tornado Genesis and Evolution from an Initial Instability Profile

Alexios Nicolas Philippou[a, b]

K. M. Isaac[a*]

[a]Missouri University of Science and Technology, 400 W 13th St, Rolla, MO 65409, USA
[b]James Watt School of Engineering, University of Glasgow, G12 8QQ, Scotland, UK
[*]Corresponding author. ✉isaac@mst.edu

Missouri University of Science and Technology Technical Report

Report Number: MST_MAE_DD_2023_01
February 15, 2023

Abstract

A likely mechanism for the little-understood tornado genesis is proposed and its numerical implementation is presented. The Burgers-Rott vortex with its axis in the vertical direction is introduced as an instability mechanism, and the flow field then evolves under the influence of the atmospheric pressure, temperature and density variations with altitude. Buoyancy effects are implemented using the Boussinesq model. Results are presented and discussed for a set of conditions including mesh type and size, different turbulence models, and a few different boundary conditions. Post-processed results of the transient simulations including animations contain a wealth of information to help analyze tornado behavior. Velocity contours, pressure contours, vorticity contours, streamlines, and iso-surfaces show the evolution of a complex flow field possessing many characteristics of a tornado. At longer times from the start, the flow field becomes more asymmetric with the vortex core becoming more twisted, and the eye of the vortex drifting away from the axis of the computational domain. The single initial vortex then transitions into multiple vortices of varying size and orientation. These high Reynolds number ($Re_\Gamma \sim 10^9$) simulation results show flow fields that resemble highly unsteady, massively separated turbulent flows with eddies at a wide range of spatial scales.

Keywords: Tornado CFD simulation, Mars dust devils, tornadogenesis, evolution, decay.

1. Introduction

Driven by the atmosphere getting warmer over the past few decades, tornados have become common lately. The mechanisms that cause tornados to form and evolve into sometimes destructive forces are still not well understood due to the large number of factors involved. Davies-Jones, Trapp and Bluestein (Davies-Jones, et al., 2001) have defined a tornado as a violently rotating, narrow column of air, averaging about 100 m in diameter that extends to the ground from the interior of a cumulonimbus cloud that appears as a condensation funnel pendent from the cloud base and/or as swirling cloud dust and debris. A condensation funnel that fails to reach the ground is called a funnel cloud. A waterspout is a tornado over a body of water. They divide tornados into two types. A type I tornado forms within a mesocyclone, a large scale parent circulation. In their view, to a first approximation, the tangential winds in a mesocyclone can be modeled as a Rankine Combined Vortex (RCV), with a core diameter of ~5 km. A supercell, that sometimes accompanies a mesocyclone, is a long-lived (< 1 hr) thunderstorm that has a strong spatial correlation to its parent mesocyclone and updraft. The level of precipitation from supercells influence the formation and nature of tornados, most notably the occurrence of precipitation downdraft. According to their description, a type II tornado is not associated with mesocirculation. It is generally a small and weak vortex that forms along a stationary or slowly moving wind-shift line from the rolling up of the associated vortex sheet into individual vortices. Lack of a strong parent updraft precludes it from intensifying into a strong tornado. They categorize smaller scale dust devils as probable type II tornados. They cite numerous references based on time-laps photography of tornados in the field that have documented the presence of rotation in the mesocylone. They cite recent estimates, which show that approximately 25% of radar-detected mesocyclones produce tornados. Based on the analyses by various authors, they give an estimate for the vertical vorticity of a mesocyclone ~0.01 (1/s), which is considered a benchmark by meteorologists. Davies-Jones and Brooks (Davies-Jones & Brooks, 1993) argued that an ‘in, up and out’ type of circulation driven by forces primarily aloft would fail to produce

rotation close to the ground because vertical vorticity is produced in rising air. It seldom produces damaging winds at ground level without an accompanying downdraft. They observe that tornados usually do not occur in the absence of rainy downdraft. A cool downdraft affords the baroclinic generation of horizontal vorticity in the form of a toroid that wraps around the downdraft.

Trapp and Davies-Jones (Trapp & Davies-Jones, 1997) used a set of equations to model the two-dimensional, axisymmetric forced convection inside a closed impermeable cylinder that rotated at a constant rate. A variable, $\nu \propto 1/\mathrm{Re}$, having a constant value = 0.0005, was used to model the Reynolds stresses. Motion relative to the tank was initiated by a time-dependent buoyancy field. Results were obtained for free-slip and no-slip boundary conditions. A time-dependent Burgers-Rott Vortex model provided analytical solutions that could be compared to the numerical solutions. The goal was to use results from tornado vortex chamber (TVC) experiments as a starting point to explore tornado genesis in nature, and to test under what conditions their dynamic pipe model (DPE) would be applicable. They proposed two modes for tornado genesis, labeled mode I and mode II, depending on whether the vortex originates in the supercell and extends to the ground (mode I) or the vortex initially forms on the ground and intensifies with time (mode II). They allude to treating buoyancy in a framework that doesn't distinguish between very cold air present in the supercell that will flow downward or warm air below that'll flow upward, and that the updraft or the downdraft in a tornado will be the net result of buoyancy force and the vertical pressure gradient force (VPGF). These arguments are consistent with the Navier-Stokes equations that include the pressure gradient term and the buoyancy term, in which each of these terms will influence the direction of motion depending on their relative magnitudes, and the direction of the respective forces that arise.

Tornado research is challenging because of the associated large geometric scales. Experimental studies of tornados are usually conducted on scale models (Ward, 1972) (Cardno, 2022) (Kuai, et al., 2008) (Zuo, et al., 2021) (Refan & Hangan, 2016), where the main features of tornados such as swirl, flow in the vertical direction and horizontal translation have been included. The recently completed tornado simulator at the Missouri University of Science & Technology (Cardno, 2022), reportedly the largest in the Americas, has been designed for optimal aerodynamic performance, and is mounted on overhead rails to simulate tornado translation. Flow field measurements of natural tornados have been limited due to the challenges is making measurements. A recent data set from the Spencer Tornado (Wurman & Alexander, 2005) based on radar data provide velocity profiles that have been incorporated in numerical simulations for specifying boundary conditions (Kuai, et al., 2008). Computational fluid dynamics (CFD) simulations rely on laboratory measurements and radar date from full scale tornadoes for validation. Numerical simulation of natural tornados is challenging due to their geometric scale and the need to include many factors that influence tornado formation and evolution. There are two main approaches to numerical simulation of tornados: one favored by atmospheric scientists who study aspects such as super cell formation, moisture content, and rain, to virtually create tornadoes. The details of one such model are given in (Bryan & Fritsch, 2002).

Tornado simulations based on the conservation mass, momentum and energy equations, and other equations to model the fluid (e.g., such as in multiphase flow), turbulence through turbulence model equations, and other equations that will be included for the specific problem being solved, fall under computational fluid dynamics (CFD) techniques. The set of the relevant partial differential equations are solved by various techniques. CFD simulations of laboratory-scale tornadoes with an air inlet at the bottom of a cylindrical chamber, and driven by fans at the top, have been conducted by many researchers (Kuai, et al., 2008) (Yuan, et al., 2019) (Natarajan & Hangan, 2012) (Ishihara & Liu, 2014) (Verma & Selvam, 2020). The Lewellen group has published extensively on various aspects of tornado behavior, including tornado simulation at the geometric scale of natural tornadoes (Rott & Lewellen, 1966) (Lewellen, 1993) (Lewellen, et al., 1997) (Lewellen & Lewellen, 2007) (Lewellen, et al., 2000). Their domain size was 1000 m x 1000 m x 1000 m. They used the Large Eddy Simulation (LES) turbulence model. Their focus was on the "corner flow" at the outer boundary of the inner vortex close to the ground. In this corner flow region, the radial flow toward the center is forced to turn upward in the axial direction, transitioning to an axial jet. The pressure boundary condition was approximated as that set by the cyclostrophic balance in the cylindrically symmetric region above. They used $r_c=\Gamma_\infty/V_c$ as the characteristic length scale for plotting the results in non-dimensional form. As an example of reasonable physical values, they used the following data: velocity at the core radius V_c = 75 m/s, circulation at $r \to \infty$, Γ_∞ = 15,000 m^2/s, yielding core radius r_c = 200 m. The corresponding Reynolds number Re (= Γ_∞/ν) ≅ 1.014x10^9, where ν is the kinematic viscosity. Kuai et al. (Kuai, et al., 2008) performed numerical simulations of a laboratory tornado simulator and a scaled-up version of the geometry to compare the results to radar data from the Spencer Tornado (Wurman & Alexander, 2005), by conducting steady state, three-dimensional numerical simulations. Simulation results were compared to velocity measurements using Doppler on Wheels (DOW) radar data and a pressure probe-based velocity data from the laboratory tornado simulator. Their focus was on near-ground flow field and the effect of surface roughness on maximum velocity and core radius. They used the RNG-k-ε turbulence model with wall functions. They confirmed the observations in previous studies which showed a reduction in maximum velocity with increase in roughness. Positive radial velocity (directed away from the axis) observed in the radar data was also present in the simulation results. A large data set was generated to perform sensitivity studies of parameters that included mesh size, roughness height, swirl ratio, and others. With the inlet velocity boundary conditions derived from the velocity data from the Spencer Tornado, the simulation results agreed fairly well with the velocity profiles from the field measurements. Verma and Selvam (Verma & Selvam, 2020) performed numerical simulations of the flow in a laboratory vortex chamber (Tang, et al., 2018), and their results showed temporal and spatial displacement of the vortex core, highlighting the dynamic nature of the tornadic flow field. They also observed a reduction in peak velocity with increase in surface roughness. Liu and Ishihara (Ishihara & Liu, 2014) solved the time-averaged, axisymmetric Navier-Stokes equations with LES turbulence model for a vortex chamber flow field. Natarajan and Hangan (Natarajan & Hangan, 2012) used a moving-wall boundary condition to also capture the effects of tornado translation.

In wind engineering, the Computational Fluid dynamics (CFD) simulations involve solving the equations of the conservation of mass, momentum, energy, turbulence model, and other equations that would be necessary when more complex models are used. Models for liquid phase (rain) and solid phase (dust, hail) are necessary when these phases will be present in addition to the gas phase (air, CO_2, etc.). CFD simulations require realistic initial conditions and boundary conditions to provide meaningful results. Formulating and applying physics-based boundary conditions and initial conditions are much more challenging in nature-scale tornado simulations than at laboratory-scales, where the laboratory tornado simulator in the shape of a chamber with a velocity inlet (Kuai, et al., 2008) (Yuan, et al., 2019) and a velocity outlet present in some designs (Ward, 1972) (Tang, et al., 2018) are modeled. The well-defined inlets and outlets and solid surfaces of the laboratory tornado simulators are relatively easy to implement in CFD simulations.

The goal of this work is to investigate how tornados evolve under realistic atmospheric conditions when an initial instability is introduced in a computational domain (Fig. 1) with open boundaries except for the ground which is treated as a solid surface. The scope of the study is limited to gas phase (air) only and the incompressible flow regime with the Boussinesq model for density variations with temperature. The Boussinesq model allows having buoyancy force included in the momentum equation. Important aspects of CFD simulations such as CFD domain size, mesh size and mesh distribution, and choice of turbulence model are addressed. A secondary goal is to build a framework to study dust devils on Mars which are closely related to terrestrial tornados (Reiss, et al., 2013).

Following this Section 1 introduction, Section 2 discusses details of the simulations. Section 3 covers results and discussion. Section 4 draws conclusions of the study including suggestions for future work.

2. Materials and methods

2.1 Computational domain and mesh

The shape of the computational domain is a circular cylinder (600 m diameter (D) x 600 m height(h)), Fig. 1. A cylindrical geometry was chosen because it is better suited for simulations of flow fields with a strong swirl component. The bottom boundary is a solid surface representing the ground. The side and the top are open boundaries. The meshes was created using the software platforms ANSYS and PointWise. The structured hexhedral mesh (Mesh 1) has 3.6 million cells. The unstructured mesh (Mesh 2) has ~2.3 million cells. The mesh is finely spaced in the z-direction at the bottom surface with the first cell height of 0.2 m. The cell height in the z-direction increases based on a growth factor specified during meshing.

The simulations were performed on a workstation running on an Intel 11^{th} Generation i-9 processor with 2.6 GHz CPU speed and 8 cores, and two other workstation with comparable computing power. The simulations used the parallel processing option using 4 processes. The display adaptor is an NVIDIA GeForce RTX 3080 Laptop GPU.

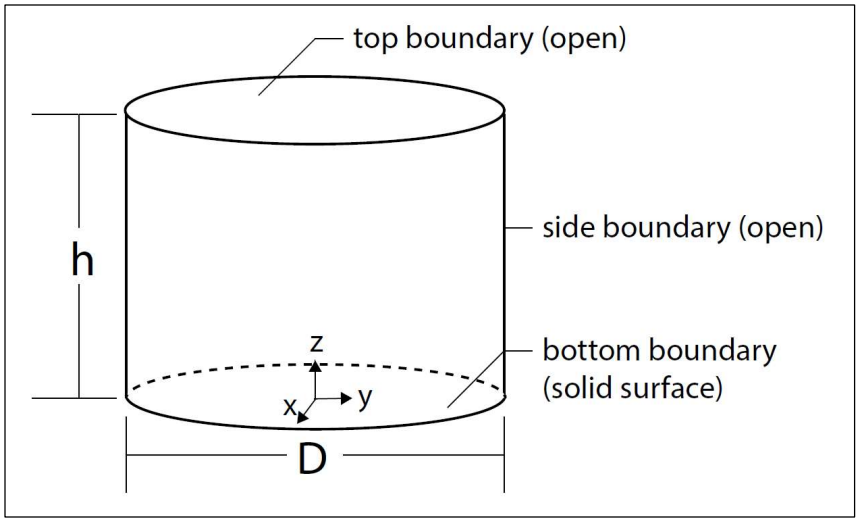

Figure 1. Circular cylinder-shaped computational domain.

2.2 Governing Equations and CFD algorithm

The CFD algorithms available in ANSYS Fuent are used to solve the Navier-Stokes equations that govern flow. For the simulation of natural tornados, where a Reynolds number can be defined as

$$\mathrm{Re} = \Gamma / \nu \tag{1}$$

where Γ is the circulation calculated at the core radius (r_c) and ν is the kinematic viscosity. In the present simulations $\mathrm{Re} \approx 10^9$, which is larger by a factor of ~100 compared to the Reynolds number of typical laboratory simulations. The time-dependent nature of the tornado flow field requires a transient formulation of the governing equations. The equations for the conservation of mass, conservation of momentum and the turbulence model are numerically solved on the mesh created during the pre-processing step.

The equations for incompressible flow are as follows.

Conservation of mass

$$\frac{\partial u_i}{\partial x_i} = 0 \tag{2}$$

Conservation of momentum

$$\frac{\partial u_i}{\partial t} + u_j \frac{\partial u_i}{\partial x_j} = \frac{1}{\rho} \frac{\partial \sigma_{ij}}{\partial x_j} + f_i \tag{3}$$

where the instantaneous velocity u is the sum of the mean value and the fluctuating component: $u = \overline{u} + u'$. σ_{ij} is the stress tensor, and the last term on the right-hand-side, f_i represents the body

force, which in this paper is the buoyancy force resulting from the Boussinesq model for incompressible flows having temperature-dependent density variations. For Newtonian fluids, the time-averaged form of Eq. 3 (denoted by overbars) becomes

$$\frac{\partial \overline{u}_i}{\partial t} + \overline{u}_j \frac{\partial \overline{u}_i}{\partial x_j} = -\frac{1}{\rho}\frac{\partial \overline{p}}{\partial x_j}\delta_{ij} + \frac{1}{\rho}\frac{\partial}{\partial x_j}\left[\mu\left(\frac{\partial \overline{u}_i}{\partial x_j} + \frac{\partial \overline{u}_j}{\partial x_i}\right) + \tau_{ij}\right] + g_i \tag{4}$$

where g represents gravity, δ_{ij} is the Kronecker delta, τ_{ij} is the Reynolds stress tensor ($\equiv -\rho \overbrace{u_i' u_j'}^{\text{time averaged}}$).

The energy equation can be written in terms of the temperature T for an ideal gas as follows.

$$\frac{\partial T}{\partial t} + u_j \frac{\partial T}{\partial x_j} = \alpha \frac{\partial^2 T}{\partial x_j \partial x_j} \tag{5}$$

where α is the thermal diffusivity. For incompressible flow, the Boussinesq model gives an expression for density variations with temperature.

$$\rho = \rho_0 \left[1 - \beta(T - T_0)\right] \tag{6}$$

where β is the thermal expansion coefficient, and the subscript $_0$ refers to the reference value. The Boussinesq model is fairly accurate for small temperature variations from the reference temperature.

As the Reynolds stress tensor τ_{ij} is symmetric, it has six unknown components. The three diagonal ($i = j$) components are normal stresses and the other three are shear stresses. Since the number of equations represented by Eqs. 2 and 4 are fewer than the number of unknowns, it gives rise to the 'closure problem' in turbulent flow. Vastly researched turbulence modeling techniques are a way to address the closure problem.

Turbulence model

The wall model LES (Shur, et al., 2008) is used for many of the results presented here. The Spalart-Allmaras (SA) one-equation turbulence model (Spalart & Garbaruk, 2020) has also been used in some cases to compare to WMLES and to evaluate its suitability. The large eddy simulation (LES) turbulence model has been preferred by many investigators in tornado simulations due to its favorable attributes in modeling supercells. LES with subgrid scale models (Shi, et al., 2018) was not considered due to the requirement of much finer mesh--with mesh size orders of magnitude larger than used in the present study--compared to WMLES. Bose and Park (Bose & Park, 2018) estimated that the wall-resolved LES (WRLES) would require the number of grid points, $N \sim O(Re_L^{(13/7)})$, where Re_L is the Reynolds number based on the characteristic length, L. Based on a typical case from the present work, this translates to $N \sim 5.2 \times 10^{16}$ grid points in the wall-normal direction for $Re_L \sim 10^9$. Obviously, this estimate shows that WRLES would not be feasible until computing power increases by several orders of

magnitude. Wall model LES combines the RANS (Reynolds-Averaged Navier-Stokes) turbulence model for eddy scales not resolved by LES. Spalart [2009] has reviewed WMLES for several canonical flows and concluded that WMLES would be a good choice for the turbulence model for atmospheric flow field simulation, where both the wall zone and zones away from the wall are equally important for studying atmospheric phenomena such as dust devils and tornados. This compromise, of course, results in some loss of precision in calculating variables such as the wall shear stress, but the overall flow field behavior in the wall region such as the inner corner flow region (Lewellen, et al., 2000) are likely to be preserved. There are a few different versions of WMLES which differ from each other in their details. The algebraic WMLES formulation proposed by Shur et.al. (Shur, et al., 2008) combines a mixing length model with LES, and with the wall-damping function of Piomelli (Piomelli & Balaras, 2002). The detached eddy simulation (DES) (Spalart, 2009) proposed for massively separated flows is a variation of LES that combines LES and RANS models that was found to be suitable for the present study, and some of the present results are based on DES. Table 1 gives a summary of the representative simulations conducted for this study.

A significant difference between the present simulations and most of the published work on evaluations of turbulence models is the much larger Reynolds number ($\mathrm{Re}_\Gamma = O(10^9)$). The associated turbulent length scales range from O(km) to O(mm). A representative calculation of the Kolmogorov scale η (Kolmogorov, 1941) using the dissipation rate (ε) from a DES simulation with *k-ω SST* model for RANS at 30s from the start, at a point midway between the ground and the edge of the boundary layer, shows that $\eta = 4.791$ mm, calculated using the expression (Pope, 2000)

$$\eta = \left(\frac{\nu^3}{\varepsilon} \right)^{1/4} \tag{7}$$

Where ν is the kinematic viscosity. Considering that the largest length scale would be $O(r_c)$, where r_c (~60 m) is the core radius during the early part of the process. These estimates give a ratio of the largest to the smallest scales O(60,000). They further confirm that LES with RANS-based subgrid scale modeling would be a realistic option for simulations such as the present.

2.3 Domain Selection and Boundary Conditions

A primary objective of the present study is to critically examine the domain size and the boundary conditions used in the simulation of natural tornadoes. Choice of these parameters in previous simulations have shown significant influence on the results, and they must be chosen after careful comparison of the simulation results with available field observations and measurements. Three domain sizes were considered for a fixed height h = 600m, and diameter D = 200m, 300m and 600m. The goal of varying the diameter and keeping the height constant was to observe the aspect ratio (h/D) on the results. Analysis of a few runs showed that 600 m diameter domain gave results that were qualitatively closer to field observations. Therefore, the subsequent simulations were done using the domain having h/D = 1.

Another primary objective was to properly specify the boundary conditions that are closer to the physics of natural tornados. One way to specify the boundary conditions is to have a velocity inlet, for example, on the curved side boundary in Fig. 1, and specify a tangential velocity component and a radial velocity component based on a selected swirl ratio, that are constant with time. Such a boundary condition specification provides a continuous driving force for the evolution of the tornado starting with the initial conditions. Under this formulation, the tornado will reach a steady state, and will not undergo the birth, growth and decay observed in natural tornados.

In the present study, we have implemented an alternate approach that is closer to the properties of the atmosphere, specifically that of the Standard Atmosphere, published by organizations such as the International Civil Aviation Organization (ICAO). Under this boundary condition formulation, after the tornado is born due to an instability, it is driven by the variations of the pressure, temperature and density in the atmosphere. One scenario in which atmospheric instabilities that spawn tornados is discussed under Initial Conditions section (§2.4). Following this reasoning, we have chosen the side boundary and top boundary to be pressure boundaries in the Fluent CFD solver (Ansys, Inc., 2022), where the flow direction may be into the domain or out of it, a result determined by the solution.

The bottom boundary (Fig. 1) is usually a solid surface (ground) where the no-slip boundary condition is applied with appropriate turbulence parameters to account for the conditions of the terrain such as its "roughness."

2.4 Initial conditions

Since tornados form as a result of favorable atmospheric conditions, the initial conditions that must be specified for a CFD simulation plays a crucial role in capturing the essential behavior of tornados. Tornado genesis is perhaps the least understood aspect of tornados, and, lately, it has been a focus for researchers to gain greater insight into it. Beyond the basic understanding that instability mechanisms such as horizontal and vertical wind shear create favorable conditions for tornado formation as often mentioned in weather forecasts, many specifics are still unknown. In some previous studies, a vortex has been used to introduce an initial instability mechanism (Gillmeier, et al., 2018). The Rankine Combined Vortex (RCV) and the Burgers-Rott Vortex (BRV) (Rott, 1958) have been considered to introduce an initial instability in modeling. The RCV model has a core which rotates with a linear velocity variation (rotational flow) along the radius, and then transitions into a free vortex (irrotational flow) at certain radial distance known as the core radius (r_c). The RCV has a slope discontinuity at the core radius. Both RCV and BRV do not have radial and axial velocity components. Gillmeier et al. (Gillmeier, et al., 2018) have discussed vortex models having radial (r) and axial (z) components of velocity, in addition to the tangential (θ) component, obtained from inviscid axisymmetric, swirling stagnation point flow, which satisfies the continuity equation. However, their model is not used in the present simulations, since the magnitudes of the radial and axial components go to ∞ as r and z tend to ∞, respectively, in the inviscid stagnation point flow model. Instead, the radial and axial

components of the velocity evolve with time starting from t = 0, governed by the Navier-Stokes equations (4) and the turbulence model equations.

The Burgers-Rott Vortex is physically more realistic compared to RCV, with no slope discontinuity at the core radius where it transitions from rotational flow to irrotational flow. The RCV and BRV core radii can be defined as the radial location of the maximum velocity. In the

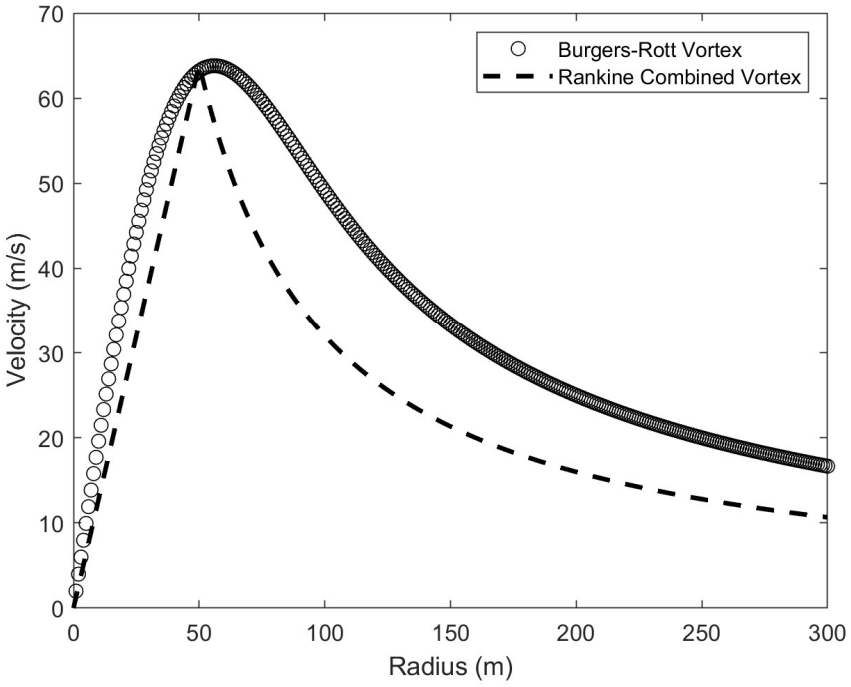

Figure 2. Burgers-Rott Vortex (BRV) and Rankine Combined Vortex (RCV)

presented results, the BRV is used to introduce an initial instability. A few simulations initialized with RCV gave results very similar to those from BRV initialized simulations. One possible mechanism for the formation of a BRV-like vortex is a horizontal wind shear as shown in Fig. 3. The up and down arrows could form a clockwise vortex resembling a BRV. With the BRV as the initial condition, the flow field evolves under the influence of the boundary conditions specified at the bottom, side and top boundaries of the computational domain (Fig. 1) into a tornado-like flow with attributes similar to a natural tornado. Thus, the key difference from previous approaches is the source of the driving force, the natural atmospheric pressure, temperature and density variations with altitude used in the present simulations, instead of the inlet velocity used as a boundary condition.

3. Results and Discussion

3.1 Reynolds number considerations

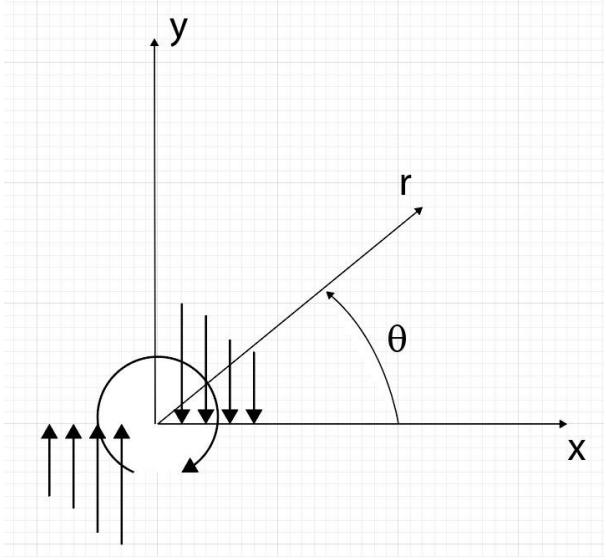

Figure 3. Wind shear as a possible mechanism for vortex formation. The arrows on the left and right of the y-axis indicate wind direction.

Numerical simulations of the Navier-Stokes equations to investigate tornados fall mainly into two groups. In the first, the simulations are modeled after laboratory tornado simulators, the largest one of which are few meters in height and diameter (Kuai, et al., 2008) (Cardno, 2022). The typical geometry can be described as a domed cylindrical chamber raised from the floor such that the rim of the chamber is at a certain height, with the gap between the floor and the rim serving as the air inlet. The flow is induced by a blower mounted at the top of the dome. A strong swirl velocity component is induced by the blower and guide vanes. The guide vanes increase the blower efficiency and provide a smooth swirling flow at the outlet. The domed enclosure is used to circulate the flow. In this closed loop design, conservation of mass considerations lead to the radial component of velocity at the inlet being nearly zero under steady state operation.

The well-defined geometry of the laboratory simulator having an inlet, (and an outlet, depending on the design) and solid walls helps define the computational domain and boundary conditions with little ambiguity. The maximum Reynolds number of a large laboratory simulator would be $Re_{\Gamma} \sim 50 \times 10^6$. The Reynolds number associated with a typical natural tornado will be $Re_{\Gamma} \sim 10^9$, as will be seen in the simulation details given in later sections. The Reynolds number of natural tornadoes, larger by orders of magnitude, should be considered in the selection of the computational domain, mesh size and the turbulence model.

3.2 Overview

The size of our computational domain (D = 600m, h = 600m) is the same order of magnitude as the size of natural tornados as reported in literature (Lewellen, et al., 1997). The initial conditions and the boundary conditions are axisymmetric. However, the governing equations are for unsteady, three-dimensional flow, and the solution gives rise to a transient, three-dimensional flow field. As the solution progresses in time, the 3D aspects become more prominent. Solutions for a time span of up to 140 s were obtained. The following sections will describe numerous features of the tornado observed in the different cases that were run.

Table 1 Simulation Case Summary

Case name	Mesh type	Mesh cell number	Turbulence model	Δt (s)	Buoyancy?	Comments
Case 02	Unstructured	2.62×10^6	SA	0.01	No	
Case 08	Unstructured	2.62×10^6	WMLES	0.01	No	
Case 08b	Structured	3.6×10^6	WMLES	0.01	Yes	
Case 09	Unstructured	2.62×10^6	WMLES	0.01	No	p(z) constant
Case 10	Structured	3.6×10^6	SA	0.01	Yes	Funnel cloud
Case 11	Structured	3.6×10^6	WMLES	0.01	Yes	ΔT_G = +10K
Case 12	Structured	3.6×10^6	DES/SA	0.01	Yes	
Case13	Structured	3.6×10^6	DES/k-ω	0.01	Yes	
Case 17	Structured	3.6×10^6	DES/SA	0.01	Yes	8 cores. $\varepsilon = 10^{-4}$

Notes: ΔT_G - Differential ground temperature. ε – residual setting for convergence

Table 1 shows the summary of representative simulations completed in order to understand the nature of the solutions under the selections in the table. These include mesh size, mesh type (structured vs. unstructured), turbulence model, integration time step, inclusion of buoyancy, no pressure variation with altitude, number of computer CPU cores, and convergence criteria set by residuals. Both the mesh sizes used in the simulations were found to give solutions that are largely mesh-independent with some differences in details such as the shape of the contours in the contour plots. The differences between structured and unstructured mesh were in the slightly larger number of iterations for convergence for the unstructured mesh, and the structured mesh yielding smoother appearance in the post-processed results. Simulations were run with 1, 4 and 8 CPU cores to compare differences in processing speeds. Using 4 and 8 cores provided shorter CPU time/iteration. Most of the simulations used 4 cores. as processing speeds were less critical compared to the time needed to post-process the results, no attempt was made to optimize the number of cores for minimum time per iteration. Setting $\varepsilon = 10^{-3}$ was found to give results that closely matched those using $\varepsilon = 10^{-4}$, and therefore, most of the presented results are based on the larger value of $\varepsilon = 10^{-3}$.

3.3 Simulation Cases

Detailed results are presented from a few cases shown in Table 1. An unstructured mesh with 2,697,052 tetrahedral/hexahedral hybrid cells is referred to as Mesh 01, and the larger structured mesh with 3,600,000 cells is referred to as Mesh 02. The simulations were for incompressible, transient flow with 2nd-order implicit time integration. The time step size $\Delta t = 0.01$s was chosen to ensure time-accurate solution based on the estimate in (Frölich & Rodi, 2002). A description of the pressure-velocity coupling algorithm used in the solution known as SIMPLEC is given in (Ansys, Inc., 2022). The LES/RANS turbulence model named wall model LES (WMLES), the detached eddy simulation (DES) turbulence model with Spalart-Allmaras (SA) and SST-kω for RANS are the turbulence model used for obtaining the presented results (see section 2.2 for details).

3.3.1 Initial Conditions

The solution was initialized with the Burgers-Rott vortex (BRV) with core radius r_c = 50 m and peak tangential velocity $u_{\theta max}$ = 60 m/s. With reference to the coordinate system shown in Fig.5, the BRV axis is along the z-direction. Figure 5 shows velocity profile in the radial direction plotted after initialization showing that the BRV profile is preserved after initializing, but prior to the start of the time integration.

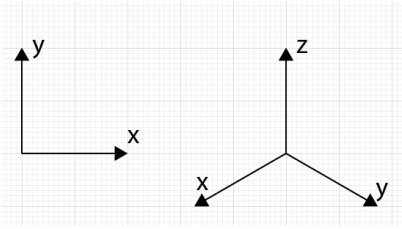

Figure 4. coordinate directions used to discuss 2D (xy) and 3D (xyz) results

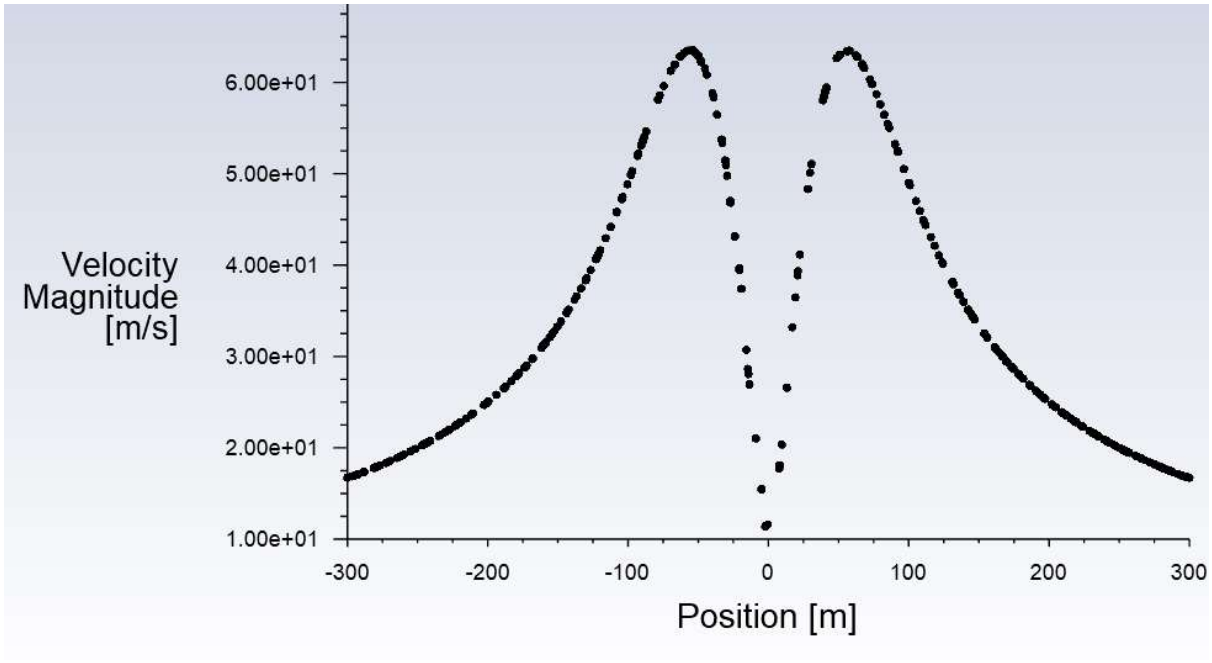

Figure 5. Burgers-Rott vortex (BRV) velocity profile (u_θ) after initialization in FLUENT. The profile shows that after initialization, the profile shape is the same that of the BRV profile used for initializing, ensuring the accuracy of the user-defined function (UDF) used for initialization.

3.3.2 Boundary conditions

The computational domain is a circular cylinder with three boundaries. The bottom of the domain is flush with the ground, and it is modeled as a solid wall with no-slip boundary condition. The thermal boundary condition is specified using temperature. Standard atmospheric pressure and temperature variations with altitude are used for the curved side boundary. Constant values of pressure with reference to the operating pressure (p = -7029.5 Pa) and temperature and T = 282.5 K obtained from the standard atmospheric data are specified at the top boundary. These pressure boundary conditions allow fluid to flow in or flow out at each boundary cell face on the side and top boundaries as the solution warrants, thereby removing a key limitation of simulations which specify the curved boundary as a slip/no-slip wall.

The Solutions converged very fast at each time step except for the initial few milliseconds. A time integration time Δt = 0.01s was used in most of the simulations. Fröhlich and Rodi (Frölich & Rodi, 2002) suggest selecting Δt based on $C = \left(\bar{u}\Delta t / \Delta x\right) \le O(1)$. The above Δt = 0.01s is in line with their recommendation. Representative values of Δx = 1 m, and $\bar{u}$ = 60 m/s, from the present simulations give C = $O(1)$.

Figure 6 shows the convergence history of a typical run. The x-axis also represents the cumulative number of iterations. The solution converged at every time step within a few (typically 2) iterations. An important feature to note is that the residuals do not increase significantly when advancing to the next time step, an indication that the flow field does not vary substantially with each time step, one more indication that the step size is small enough to accurately capture the transient flow field. A few test runs were by reducing the convergence criterion ε and the time step size Δt by a factor of 10. The results from those test runs agreed well with those from the baseline. The main difference was in the larger number of iterations per time step needed for convergence.

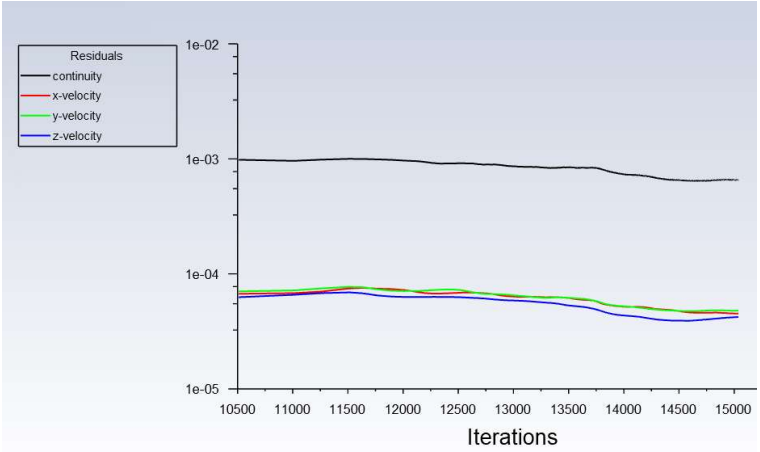

Figure 6. Residual history

3.3.3 Flow Field Static Pressure

Figures 7-10 show static pressure (gauge) contours at 1s, 20s, 80s and 120s from the start in horizontal (xy) planes at 0 m, 10 m, 50 m, 100 m, 300 m and 500 m elevations (z-coordinates) from the ground. The maximum pressure is 74.6 Pa, which is above the maximum of 0 Pa specified in the solution initialization. The minimum value is -7,650 Pa, which is 640 Pa lower than the value specified for top (z = 600 m) of the domain. At t = 1s, the contours are largely symmetric about the center with an asymmetric region in the vicinity of the 6'O-clock position,

the Figs. 9(a) - 9(e). The contours in Fig. 7(f) are quite different from those at lower elevations. They are more closely packed indicating larger gradients from the center toward the periphery. The asymmetric region around the 6'O-clock position present at the 5 lower elevations is absent in Fig. 7(f). Except for a small circular region around the center, the pressure increases toward the periphery, indicating the influence of the swirl velocity near the center. The 'eye' of the vortex is nearly the same size in Figs. 7(a) – 7(e). The 'eye' is larger in Fig. 7(f), with a more uniform low-pressure region indicated in blue. The 'eye' stays close to the center of the circular cross section at this 1s elapsed time.

Figure 8 shows the static pressure contours at t = 20s at the same elevations as in Fig. 7. The size of the 'eye' has remained nearly the same compared to the t = 1s case. The 'eye' has moved to the left (9'O-clock position). The asymmetric peripheral region has shifted to the 3'O-clock location at this instant. The z = 500 m contours in Fig. 8 (f) show significant differences from the corresponding ones in Fig. 7(f). The contours are not as tightly packed, and they have less symmetry about the center of the circle. The size of the low-pressure region indicated in blue is smaller for this case.

Figures 9(a) – 9(f) show the static pressure contours a t = 80s for the same 6 elevations as in Figs. 7 and 8. These figures show further loss of symmetry compared to previous times. The pressure levels are higher, and the 'eye' size has not changed significantly. The 'eye' has moved up to the 10'O-clock position in Fig. 9(a). Comparing the six figures in this set starting at z = 0 m to z = 500 m indicate the eye moving in a clockwise sense starting at the 10'O-clock position at z = 0, and ending near the center at z = 500 m. This would indicate a spiraling column in 3D with the 'eye' at the center of the column. It is quite revealing to note that, in spite of the initial conditions and boundary conditions being axisymmetric, there is significant loss of symmetry with increasing elapsed time (indicated by the 'eye' moving away from the center at z = 0) and with increasing altitude (indicated by the core occupying different azimuthal locations with change in altitude). Figures 9(a) – 9(d) show secondary pressure contours not enclosing the 'eye' indicating the presence of weaker secondary vortices. An animation of the pressure contours (File name: *case08b_p_stat_xy_coord_surf_80s*) (Isaac, 2023) that corresponds to those in Fig. 9, gives a continuous variation of the pressure contours in the horizontal planes.

Figure 10(a) – 10(f) show the static pressure contours at t = 120s. The contours levels show further weakening of the main vortex. The secondary vortices are further separated from the 'eye,' which is midway between the center and the periphery along a radius drawn at ~45° from the +x axis. The contours at z = 500 (Fig. 10(f)) are quite different from those at lower altitudes, probably caused by imposing the -7,030 Pa uniform boundary condition on the top boundary.

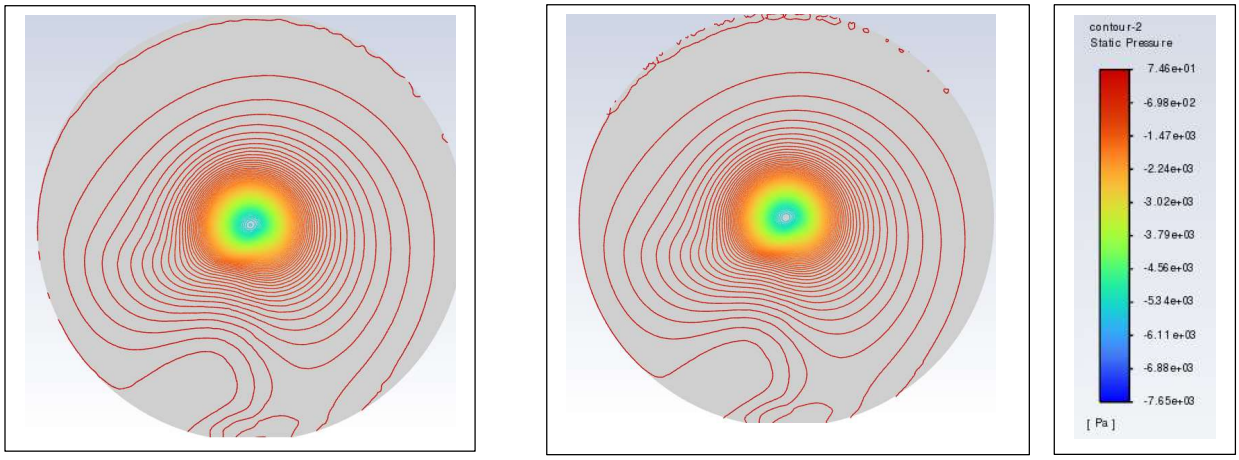

(a) z = 0 m (b) z = 10 m

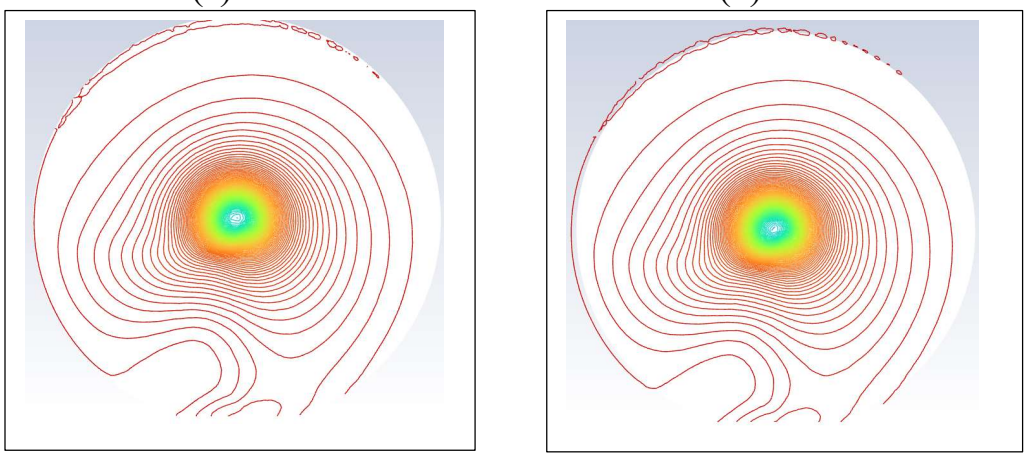

(c) z = 50 m (d) z =100

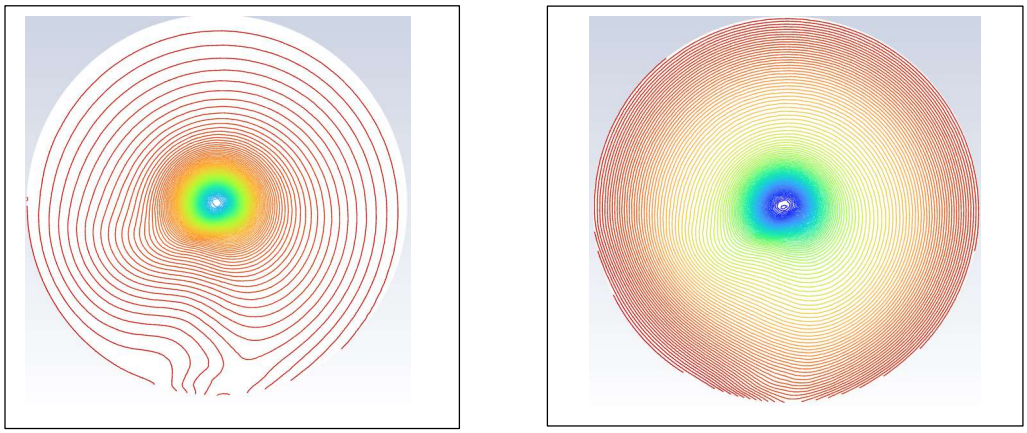

(d) z = 300 m (e) z = 500 m

Figure 7. Static pressure contours at t = 1 s.

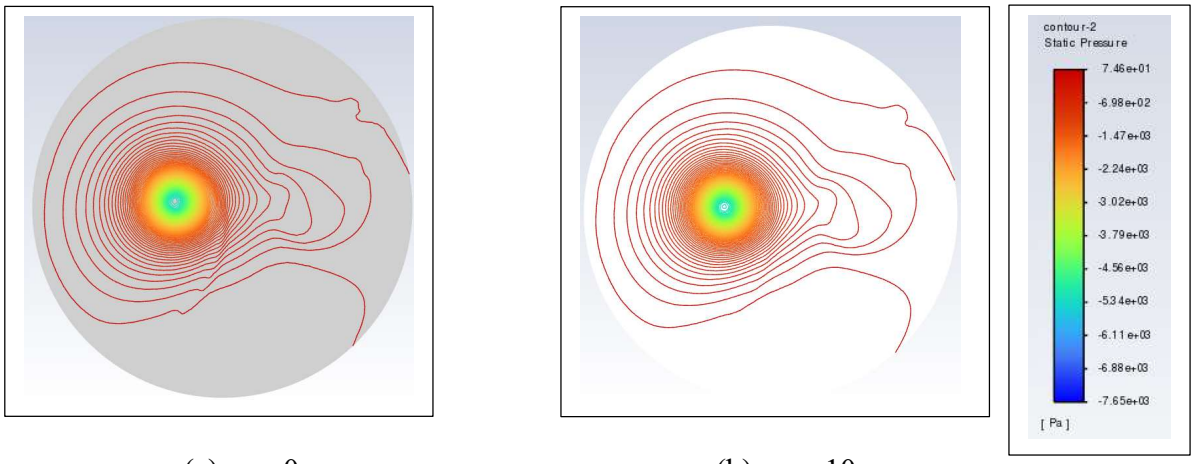

(a) z = 0 m (b) z = 10 m

(c) z = 50 m (d) z = 100 m

(e) z = 300 m (f) z = 500 m

Figure 8. Static pressure contours at t = 20 s

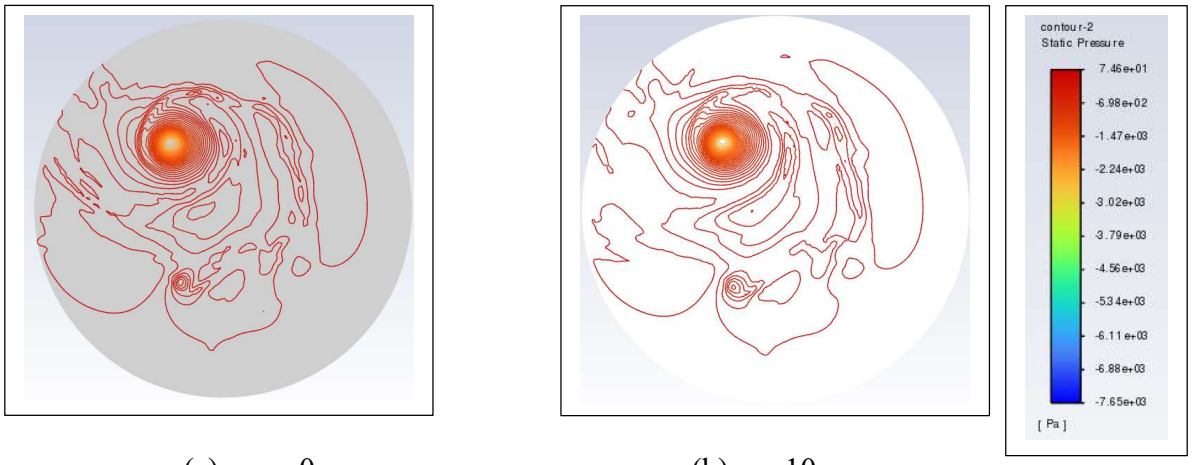

(a) z = 0 m (b) z = 10 m

(c) z = 50 m (d) z = 100 m

(e) z = 300 m (f) z = 500 m

Figure 9. Static pressure contours at t = 80 s

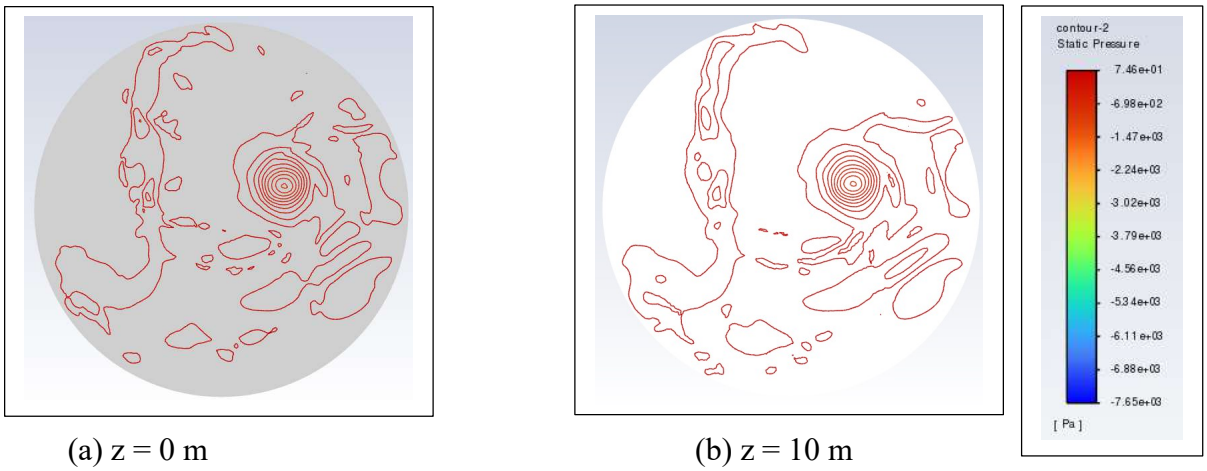

(a) z = 0 m (b) z = 10 m

(c) z = 50 m (d) z = 100 m

(e) z = 300 m (f) z = 500 m

Figure 10. Static pressure contours at t = 120 s

3.3.4 Velocity Field

Figures 11-14 show the velocity contours at the same elapsed times and altitudes as in Figs. 7 – 10. The set of velocity contours at different times and altitudes sheds more light on the dynamics of the flow structure as the flow evolves from the imposed initial conditions and boundary conditions. It can be seen from the animations (File name: *case08_pathlines_80s*) (Isaac, 2023) corresponding to these figures that the flow is counterclockwise looking in the -z-direction. There is an inflow and an outflow region in the 6'O-clock to 9'O-clock quadrant, where most of the fluid enters at the boundary, loops around the core and exits slightly below the 9'O-clock location. The velocity contours in Figs. 12-14 are helpful to approximate the core radius defined as the radius where the velocity is maximum. Since the vortical flow is not truly axisymmetric, only an estimate of the core radius can be made. The approximate value of the core radius r_c varies from ~60 m to ~72 m at t = 1s (Fig. 11). At t = 20s (Fig. 12), the core radius is ~70 m, slightly higher than at t = 1s. At t = 80s (Fig. 13), the core is further distorted from a circle, and weaker secondary vortices can be seen to form. The velocity magnitudes are lower compared to previous times, showing a drop of ~20 m/s from the t = 20s contours. At t = 120s (Fig. 14), the velocity magnitude drops further, and the weaker secondary vortices are more in number.

A discussion of the effect of swirl ratio (S) on tornado structure starting with a single axisymmetric vortex for small values of S, and the appearance of a downdraft at the axis, as S increases is given in (Davies-Jones, et al., 2001). Figure 5.29 in their article gives a graphical representation of the process showing the formation of multiple tornados. The downdraft that forms at certain altitude at small values of S extends downward as S increases, and finally reaches the ground. Since the present simulations do not have boundaries where the tangential and radial velocity components (or the swirl ratio) are specified, a well-defined swirl ratio does not exist. However, to make comparisons to other simulations where swirl ratios are specified through boundary conditions, and experiments in which S can be imposed at the inlet to the tornado vortex chamber (TVC) by using a swirl control mechanism such as variable-angle vanes, an order of magnitude swirl ratio can be calculated from the simulation results as

$$S = \frac{\overline{u}_\theta}{\overline{u}_r} \tag{5}$$

where $\overline{u}_\theta$ and $\overline{u}_r$ are the area-averaged tangential and radial velocity magnitudes in a given horizontal plane (z = constant), which, upon post-processing the simulation results, gives S = 2.26 at t = 20s and z = 300 m. Note that the swirl ratio $S = \infty$ at initialization, since the initial Burgers-Rott velocity profile is purely tangential. As time progresses, the updraft created by the negative pressure gradient and the deceleration of the flow in the boundary layer draws fluid from the side boundary resulting in a finite radial velocity component and a finite value for the swirl ratio.

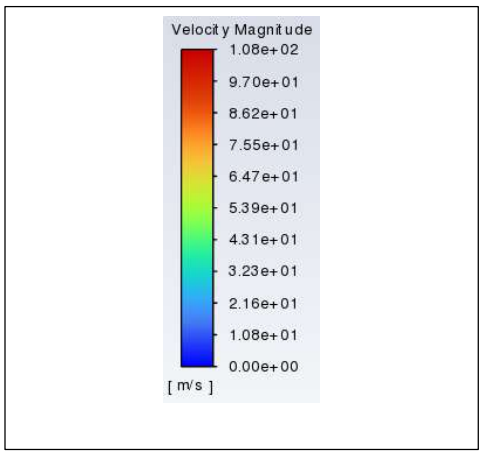

(a) Color key

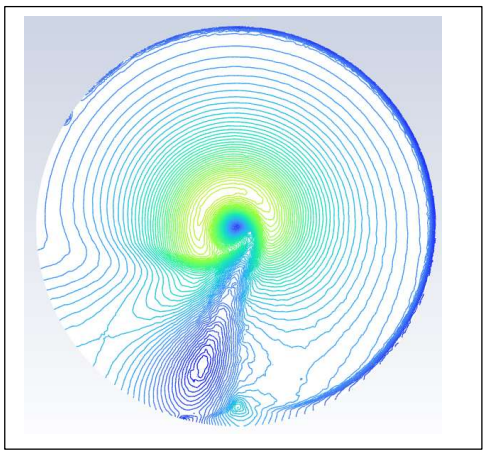

(b) z = 10 m

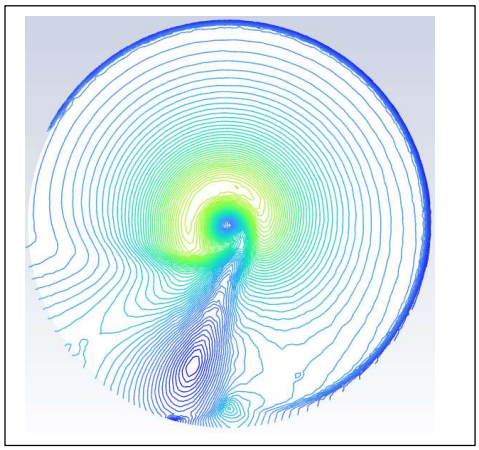

(c) z = 50 m

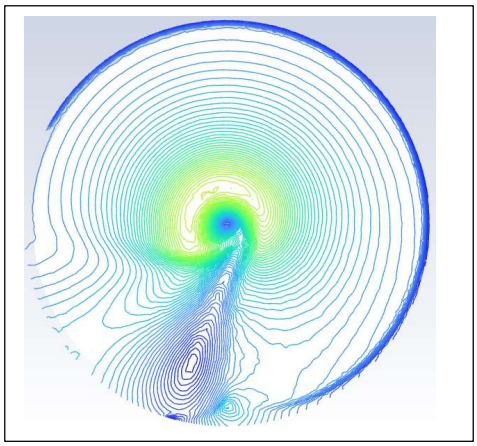

(d) z = 100 m

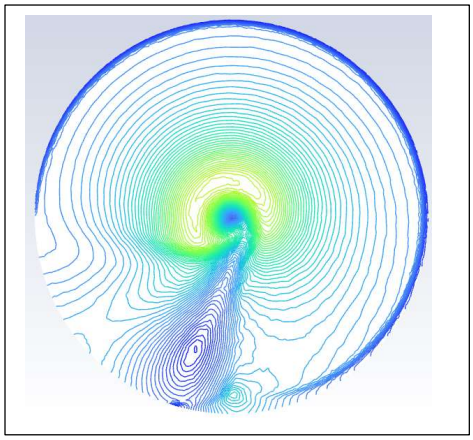

(e) z = 300 m

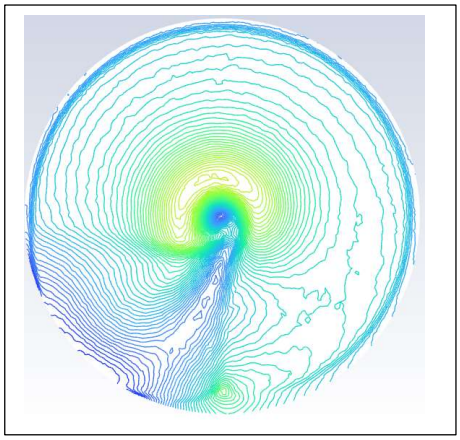

(f) z = 500 m

Figure 11. Velocity contours at 5 elevations, t = 1 s.

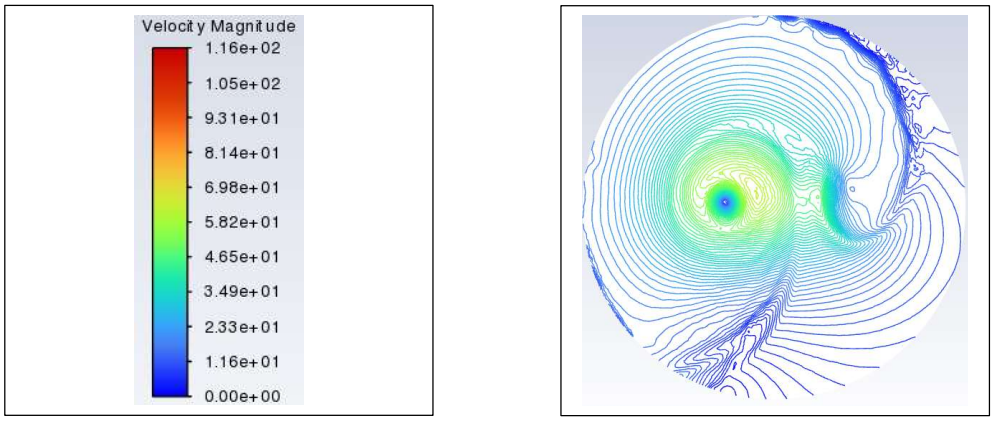

(a) z = 0 m (b) z = 10 m

(c) z = 50 m (d) z = 100 m

(e) z = 300 m (f) z = 500 m

Figure 12. Velocity magnitude contours at t = 20 s

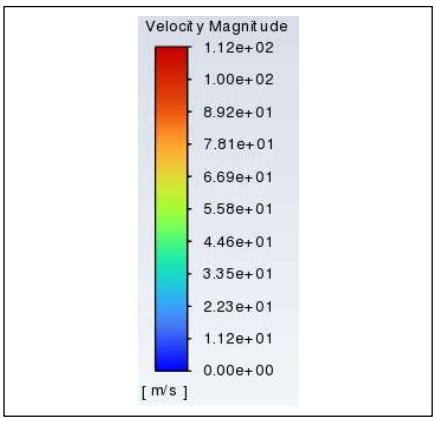

(a)

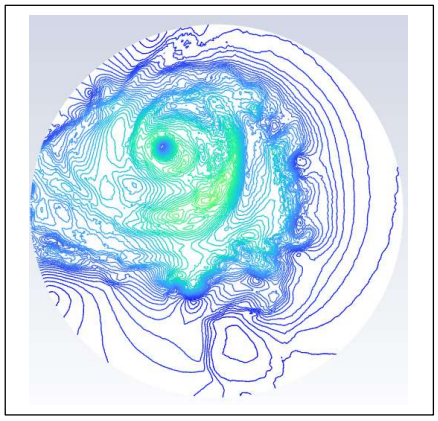

(b) z = 10 m

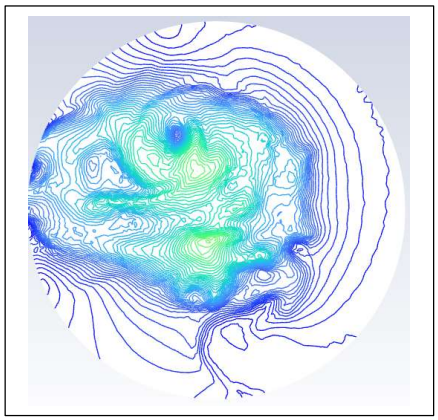

(c) z = 50 m

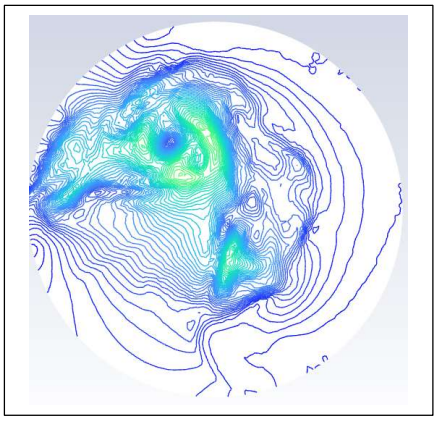

(d) z = 100

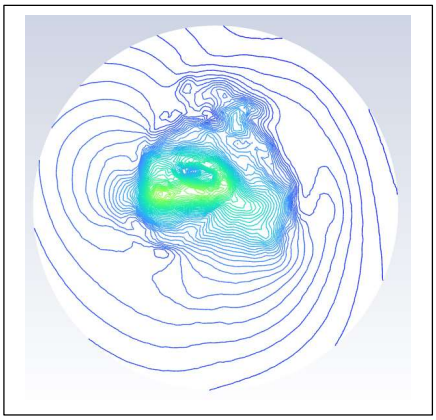

(e) z = 300 m

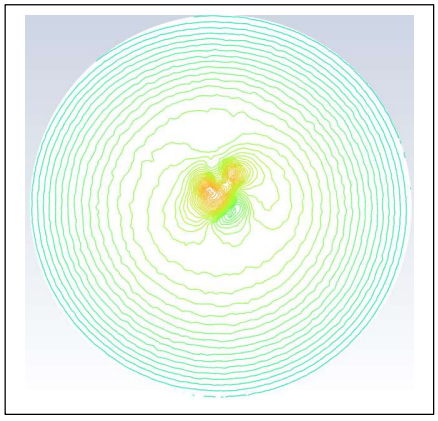

(f) 500 m

Figure 13. Velocity contours at t = 80 s

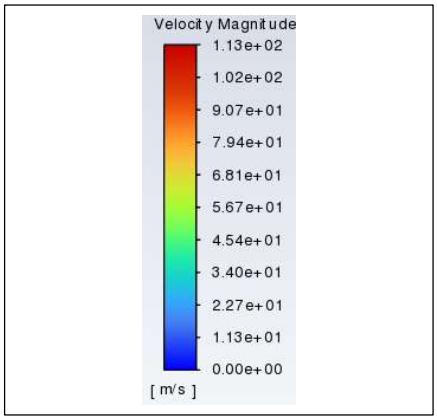

(a)

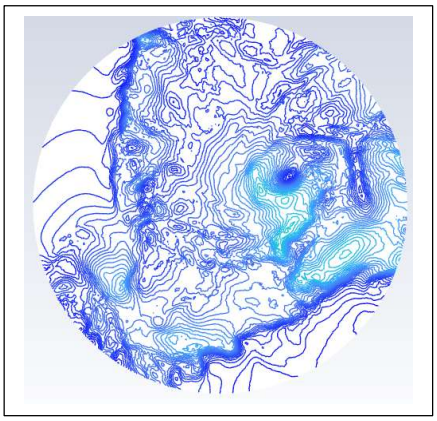

(b) z = 10 m

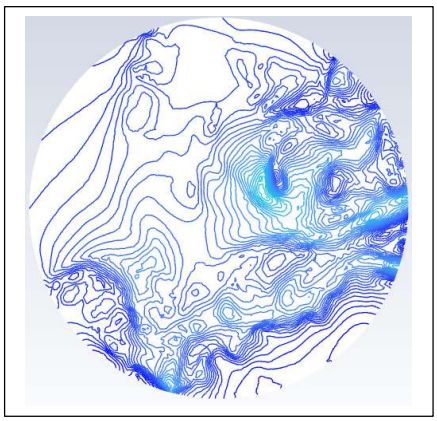

(c) z = 50 m

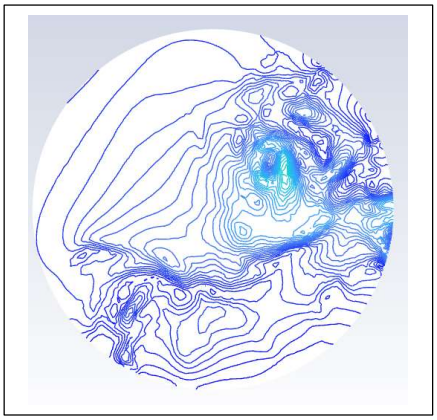

(d) 100 m

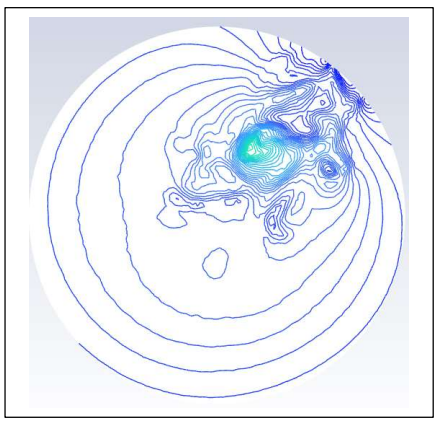

(e) z = 300 m

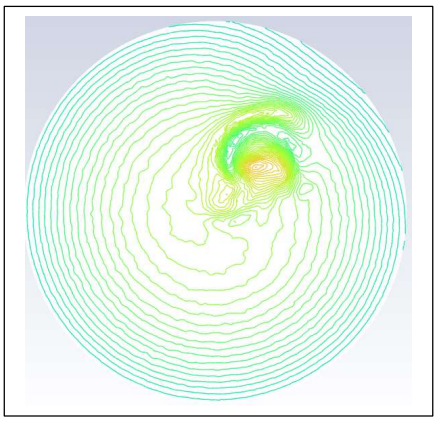

(f) z = 500 m

Figure 14. Velocity magnitude contours at t = 120 s

3.3.5 Streamlines, Three-Dimensional Vortex Structure

Figure 15 shows pathlines of particles released from two horizontal planes, xy, located at heights z = 10 m, and z = 300 m, at elapsed times 1s, 10s, 20s, 40s, 80s, and 120s from the start. The xyz coordinate directions given in Fig. 4 can be used for spatial orientation. One difference between the two sets of particle paths that correspond to z = 10 m and z = 300 m, respectively, is that the inner region that extends to the location of maximum velocity, is larger at z = 300 m compared to z = 10 m for all elapsed times from t = 1 s to t = 40 s. At t = 80 s and 120 s, the particles released from the z = 10 m plane show very irregular particle paths having no well-defined inner region. At z = 10m, the flow is largely counterclockwise (CCW) in the inner region looking from above (-z-direction) in Figs. 15 (a) to 15 (d). In the outer region of the z = 10 m particle paths, fluid enters at the top left (~10-O'clock) and exits slightly above that (~12-O'clock) forming an open loop. A small vortex indicated in blue is seen between the inlet and exit. A second difference in the pathline patterns is that the particles released from the xy-plane at z= 10 m, stay nearly in their release plane for cases 15 (a) to 15(c) (1s, 10s and 20s, respectively), with little indication of any significant upward, out of plane motion. However, for the same three cases, the particles released from the xy-plane at z = 300 m form an inner region with a significant velocity component in the +z-direction. The diameter of this inner region increases from Frame (a) to Frame (c). The outer region also has a +z-velocity component, but smaller in magnitude than the inner region. In Figs. 15 (e) and 15 (f), the particles released from the z = 10 m plane show very irregular paths with no predominant direction of rotation.

The 3D views in Figs. 15(a) – 15(f) help understand the formation, strengthening and subsequent weakening of the tornado-like flow field in the vicinity of the ground. The particle paths at the six different times are colored by velocity magnitude, starting at 1s and ending at 120s. They show the start of a spiraling motion that results in the size of the core becoming larger with elapsed time, and an increase in the velocity indicated by a larger number of pathlines colored red toward the top where the particles released from the xy-plane at z = 300 m attain the maximum velocity of ~115 m/s. This pattern demonstrates that the fluid entrained from the side of the cylindrical domain undergoes a spiraling motion and accelerates toward the top of the domain.

Closer to the ground, the flow becomes more irregular and the velocity decreases indicating a weakening of the vortex on the ground. The more axisymmetric upper region lifts farther away from the ground at larger times. A representative animation at t = 80s (File name: case08*_pathlines_80s*) (Isaac, 2023) shows a complex flow pattern. The main vortex at z = 10 m is in the ~4'O-clock position. At this time, it extends all the way to the z = 300 m plane and the core diameter increases, in agreement with observations of natural tornados which usually has a funnel shape. The center of the vortex has moved away from the axis of the cylindrical domain at z = 10 m. The maximum velocity at z = 10 m is ~45 m/s. The vortex core axis is not straight, but follows an irregular curve with the core closer to the axis of the domain at z = 300 m. Another important feature is the upward motion of low velocity fluid (~10 m/s) from the 10'O-clock position at z = 10 m, and merges with the fluid at z = 300 m. The particles released from the z = 10 m plane also show three smaller secondary vortices, each slightly tilted from the vertical

direction. Overall, the pattern shows greater mixing of the fluid between the two particle release planes at t = 80s, compared to the earlier times. Toward the top of the domain, the flow pattern is more like a strongly swirling jet, which attains the maximum velocity of ~112 m/s at the top boundary.

To further understand the flow pattern resulting from this case, additional graphical post-processing has been performed by releasing seed particles from the z = 100 m plane. Representative results are shown Figs. 16(a), 16(b) and 16(c). 50 particles were released in this case. The animations that correspond to these 3 figures (File names: *case08b_strm_lines_20s_d, case08b_strm_lines_50s_d, case08b_strm_lines_80s_c*) (Isaac, 2023) would help follow the path of each streamline, enabled by a sphere moving on each. As the number of seed particles are fewer in Fig. 16 compared to Fig. 15, certain flow field features come into greater focus. At t = 20s, a single vortex with its axis straight and parallel to the z-axis is present in Fig. 16(a). An approximate core radius of this vortex can be estimated by considering the velocity variation along a horizontal line drawn from the vortex center. The vortex is significantly displaced from the axis of the computational domain. Close to the ground, a separate, distinct region is present where the streamlines outside the vortex core wrap around the vortex axis with little upward slope. The yellowish-green color of the streamlines that reach all the way to the upper boundary indicates that the velocity magnitude at the core radius is ~80 m/s. The vortex has the funnel shape often observed when tornados form in nature. The two distinct regions of the flow field, the interior vortex region with the streamlines spiraling upward and the outer region where the streamlines are nearly in horizontal planes, is an indication that the flow field is bifurcating into two with increasing time from the start. This increase in the maximum velocity magnitude from ~60 m/s at t = 0s to ~80 m/s at t = 20s can be attributed to drop in static pressure with increasing altitude in the atmosphere.

The rotation of the Burgers-Rott vortex introduced as an initial condition produces a negative pressure gradient toward the center. This pressure gradient results in the flow field developing an inward radial velocity component u_r, and to satisfy the conservation of mass equation, a velocity component u_z will develop in the +z direction. The magnitude of u_z increases with increase in z, again to satisfy the conservation of mass equation. This explains why the streamlines close to the ground have little upward slope, but their slope increases with increase in height. This observation is further supported by the radial and axial velocity profiles at the curved side boundary shown in Fig. 17(a) and 17(b), respectively. The magnitudes of both increase with altitude, z. Note also that the u_r and u_z variations in Fig. 17 are quite non-linear, with their gradients in the z-direction growing rapidly toward the top. This non-linear variation influences the streamline shapes in Figs. 15 and 16. They transition from nearly planar near the ground to a swirling vertical jet near the top boundary.

Figure 16(b) (t = 50s) shows a very complex flow field. By this time, the two distinct regions seen in Fig. 16(a) seems to have transformed into two regions with very irregular shapes. The one to the right appears to have formed from the inner vortex in Fig. 16(a), but with the streamlines showing a very knotty pattern. They don't reach all the way to the top boundary. The second region to the left and front now has streamlines reaching all the way to the top without

significant swirl component. This is an interesting observation, which seems to indicate again the bifurcation phenomenon. At t = 80s (Fig. 16(c)) the main feature is presence of a single vortex, but with a shape not as regular as in Fig. 16(a). Close to the ground the streamlines are very irregular, not having any significant swirl except at the center. The velocity magnitude is very low in this region close to the ground. Finally, it should be noted that the apparent differences between the frames in Fig. 15 and the corresponding ones in Fig. 16 for times 20s, 50s and 80s are due to the differences in particle seeding in terms of the seeding plane and the number of seeds, as well as the two different graphical post-processors used to create the streamline patterns in Fig. 15 and Fig. 16, respectively.

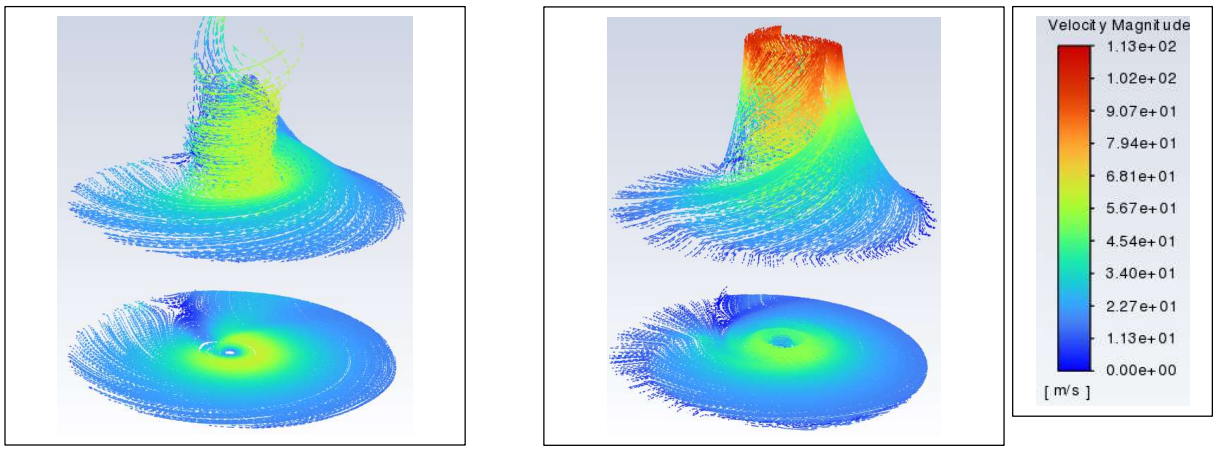

(a) t = 1 s (b) t = 10 s

(c) t = 20 s (d) t = 40 s

(e) t = 80 s (f) t = 120 s

Figure 15. Particle paths. Particles released from xy-planes at z = 10 m, and z = 300 m. Colored by velocity magnitude.

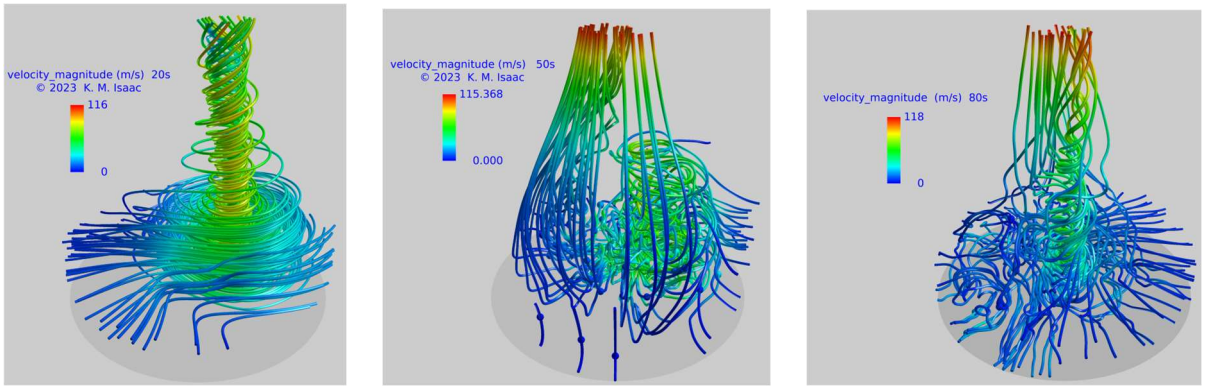

(a) (b) (c)

Figure 16. Streamlines at: (a) t = 20s, (b) t = 50s, and (c) t = 80s. Colored by velocity magnitude. The animated spheres enable better tracking of individual streamlines.

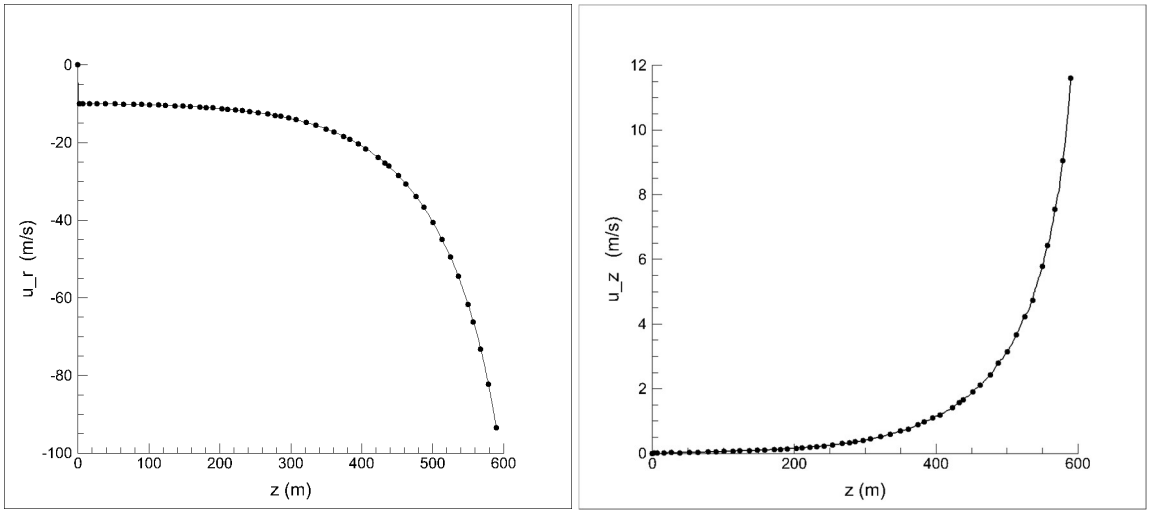

(a) (b)

Figure 17. Profiles of: (a) radial and (b) axial velocity at the curved side boundary. t = 20s.

3.3.5 Tornado-Like Flow Features

Lewellen (Lewellen, 1976) has discussed the presence of four zones in a typical tornado with particular emphasis on the inner corner flow zone on the ground. According to his description, the central vortex interacts with the radial flow toward the center. The central vortex has a stagnation point on the ground at the center, and the radial flow is superimposed on this stagnation point flow. The radial flow is decelerated in the boundary layer and turns upward creating the inner corner flow zone.

Figure 18 shows the velocity contours at t = 30s from the start. The x, y coordinate directions are shown in Fig. 4. The plane of the velocity contours in Fig. 18 is inside the boundary layer (z = 1 m), midway between surface and the edge of the boundary layer. At around this time, the flow develops the corner flow characteristics, having developed the boundary layer (profiles in Fig. 19). These profiles are at various radial locations along the x-axis (Fig. 4). The boundary layer velocity profiles should be interpreted in relation to the 'eye' of the velocity contours in Fig. 18, which has moved to the left and up from its original position at the center of the computational domain. Note that the

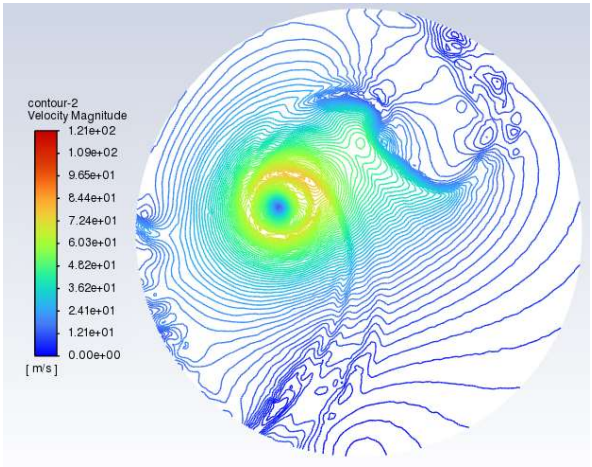

Figure 18. Velocity contours in the xy-plane, z = 1 m. t = 30s

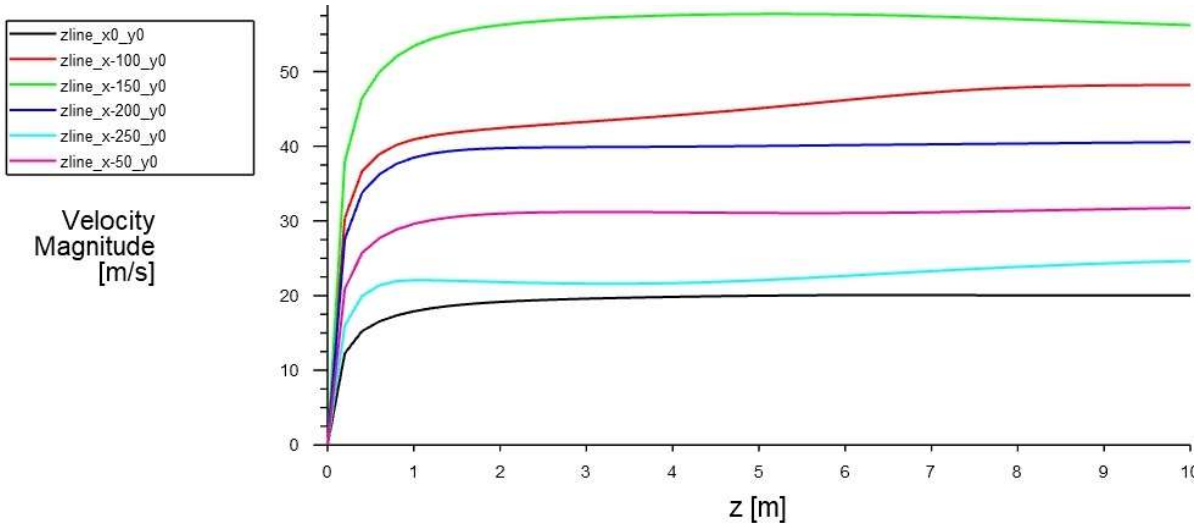

Figure 19. Velocity profiles in the z-direction including the boundary layer. t = 30s

boundary layer thickness falls in the range, δ = ~2 m – 3 m, depending on the radial location from center of the domain. The maximum velocity at the edge of the boundary layer is ~55 m/s for the x = 150 m profile (green curve, Fig. 19), which is below the maximum of the initial BRV profile.

The differences between (Lewellen & Lewellen, 2007) and the present simulations should be considered in comparing the two. They performed the simulations in two stages with two different scales for their domains. The results from the larger scale simulations are used to obtain the boundary conditions for the smaller scale tornado with the four zones. Our simulations start with the BRV initial velocity profile and no boundary layer, which develops over time, and has the profile shown in Fig. 19 at t = 30s. The other important difference is that in our simulations,

the ‘eye’ of the tornado translates whereas the ‘eye’ on the ground appears to be stationary in (Lewellen & Lewellen, 2007). This translating feature in the tornado evolution in our simulations is probably due to the boundary conditions which differ from those in (Lewellen & Lewellen, 2007). The main influence of superposing the planetary boundary layer (PBL) in our formulation is likely to be in tornado translation since the PBL can be treated as a straight-line wind due to its planetary scale compared to the size of the present computational domain. Because of the larger thickness of the PBL ($\delta = O(1\text{ km})$), it is likely to have a lower order effect on the flow near the ground compared to the thinner boundary layer ($\delta = O(2\text{ m})$) of the present simulations.

3.3.6 Vorticity Field

Figure 20 shows the contours of vorticity magnitude at z = 0 (ground). The coordinates for this 2D representation is shown in Fig. 4. The maximum value at t = 1s (Fig. 20(a)) is 27.6 (1/s). Vorticity peaks are around the core radius, but a loss of symmetry can be seen. At t = 10s (Fig. 20(b)) the maximum vorticity region is larger and forms a closed band, but the maximum value has not changed significantly. The loss of axial symmetry is due to the inflow and outflow on either side of the blue colored contours, as is clear from the particle paths in Fig. 15 (c). At t = 20s (Fig. 20(c)), the size of the high vorticity region indicated in red has diminished in size, but the magnitude is higher (32.1 1/s). At t = 40 s (Fig. 20(d)), the trend continues where the high vorticity regions get even smaller in size and the vorticity magnitude has increased to 39.1 (1/s). This trend is in agreement with previous studies (Lewellen, et al., 2000) (Davies-Jones, 2015) which have addressed tornado intensification by vortex stretching which causes an increase in vorticity and a decrease in the area of the high vorticity region roughly corresponding to the vortex core. Figures 20 (e) and 20(f) show the vorticity decaying phase where the ‘eye’ is only faintly present and the pattern is very irregular. The peak value has dropped from 39.1 (1/s) at t = 40s to 16.9 (1/s) at 120 s. These results further support the observation that the flow undergoes a transition from a predominantly in-plane motion to one with significant z-component of velocity around t = 30s, as the boundary layer develops with increase in time. It would be helpful to compare the circulation Γ from the present simulations to that from (Davies-Jones, 2015) of a mesocyclone, who estimates $\Gamma = 2$ to 6×10^5 m^2/s calculated using the line integral of velocity (21 m/s) over a circle of radius 1.5 km to 4.5 km. The present simulation gives $\Gamma = 1.06105 \times 10^4$ m^2/s obtained by integrating the z-vorticity in the xy-plane at z = 10 m. The factor of 10 difference is not surprising considering the scales of the mesocyclone and the 300 m radius domain in our calculations, as well as the difference in the method of calculating Γ between the two studies.

Figure 21 shows vorticity iso-surfaces. The frames are arranged in the order of increasing vorticity, starting with the lowest at the top left corner (frame (a-i)) and increasing to the last frame (d-iv) at the bottom right corner, where the letters represent rows and the numbers represent columns. The color key in each frame indicates the vorticity of the iso-surface in that frame. The colors in some frames are not monochrome due to the vorticity not being a single value but spread over a narrow range as indicated by the color keys. The iso-surfaces start with a vorticity magnitude $\Omega = 1.363$ (1/s) in frame (a-i) and covers a large region, wider at the bottom close to the ground and then decreasing in width with increasing height. It shows a few very

interesting features that capture the rich structure of the flow field. The lower half of the domain shows vortex tubes nearly in the horizontal plane, and the upper half shows multiple vortex tubes having axes nearly in the vertical direction. Between the lower and upper regions, there are vortex tubes having their axes directions that lie between horizontal and vertical, confirming the observations from streamline animations and other results. The iso-surfaces are very similar to those from massively separated flows over delta-wing aircraft (Spalart, 2009) at large Reynolds numbers.

In frame (a-ii), the iso-surface vorticity is 2.726 (1/s), and the surface area is smaller. The widths of the bottom and the top parts are smaller, and there is one main vortex tube in the top half. Both the halves show a few larger diameter vortex tubes and some smaller diameter vortex tubes. In frame (a-iii) for $\Omega = 4.089$ (1/s), the iso-surface area is still smaller from the previous vorticity level. The shape of the iso-surface is similar to those in the previous two frames, having a circular base close to the ground plane, a wider region of horizontal vortex tubes above it, and a column-like vortex above it. In frame (a-iv), the trend continues for $\Omega = 5.452$ (1/s) whereby the iso-surface area is smaller and the vortex tube diameters are smaller. The top single vortex tube is about to pinch off from the bottom part. A feature to note on the circular base is a narrow circular strip present between the 6'O-clock and 9'O-clock segment in Frame a-i , progressively grows in width and angular extent in the next 3 frames (a-ii)-(a-iv). This is likely to be due to the vorticity being lower there. In Frame (b-i), the iso-surface vorticity $\Omega = 6.815$ (1/s). The iso-surface area has diminished further, and the circular strip has grown larger. Two gray spots can be seen above the circular strip. The circular base shows regions consisting of spots having colors between blue and red indicating very small variation in vorticity represented in the color key. The rest of the frames (b-ii) to (d-iv) fall in a wide range $\Omega = 8.178$ (1/s) to $\Omega = 300$ (1/s). In these frames, the iso-surfaces are mostly confined to the circular base plane. These frames indicate that the high vorticity region is small and confined to the base plane close to the ground manifesting the high-vorticity in the boundary layer. The progressively smaller area of the iso-surfaces in these frames is probably an indication of the vorticity being highly non-uniform even in the boundary layer. The 12 frames in Fig. 21 taken together show the unique nature of the flow field that has evolved from the initial Burgers-Rott vortex under the influence of the pressure boundary conditions on the side and top surfaces. The near wall region shows the significant influence of the surface and the complex boundary layer that forms. Away from the ground, the flow features are similar to a massively separated flow, however, having a mean flow directed toward the top boundary.

Two animations from elapsed time t = 50s that correspond to the frames in Fig. 21, one showing iso-surfaces of vorticity (*case08b_vorticity_isosurfaces_50s_b*) and the other showing vorticity contours in the horizontal (xy) planes (*case08b_vorticity_xy_coord_surf_50s*) shed further light on the vorticity field.

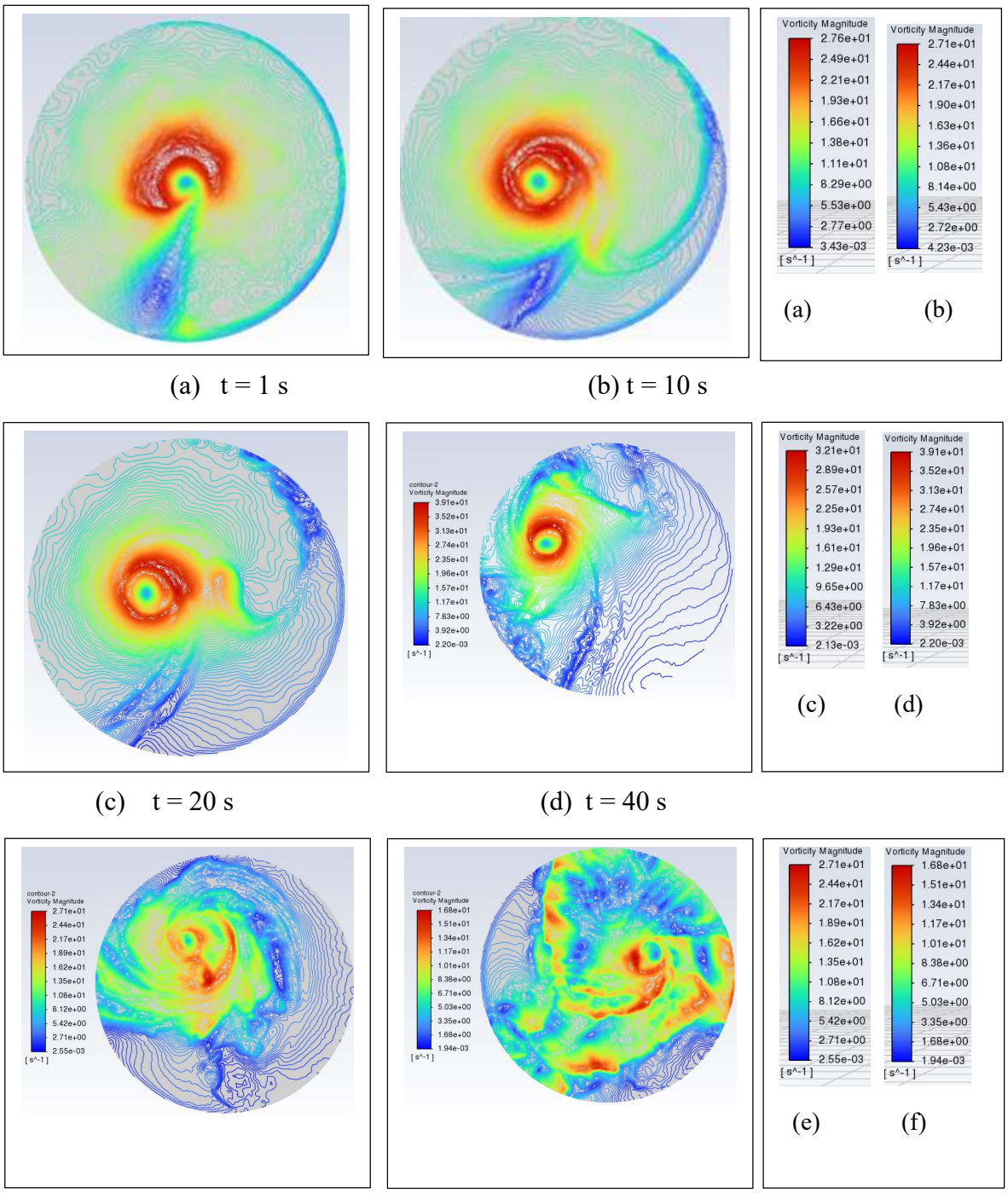

Figure 20. Vorticity contours on the ground plane.

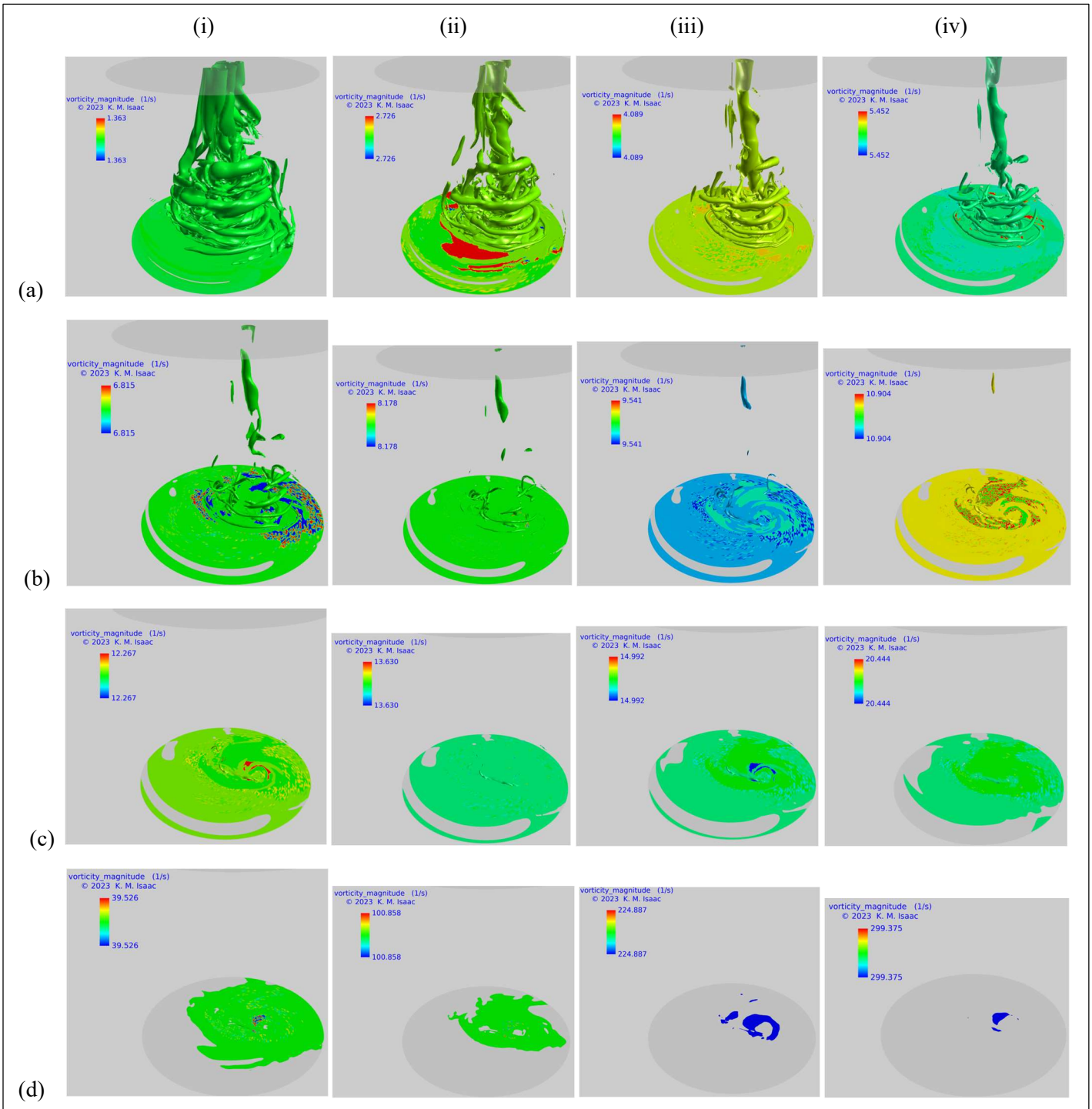

Figure 21. Vorticity iso-surfaces. t = 50s.

3.3.7 Strong Influence of Boundary Conditions

Figure 22 highlights the influence of changing the boundary conditions on the side and top boundaries to a constant pressure value of the standard atmosphere at sea-level. The corresponding animation is available at (Isaac, 2023) (File name: *case09_streamlines_30s*). The simulation is initialized with the Burgers-Rott vortex. At this elapsed time, t = 30s, the BRV vortex structure with its inner rotational core and the outer irrotational region with its axis along the z-direction, has lost its original structure, and has broken up into the highly three-dimensional structure. The streamlines show the flow field having no predominant flow direction. Noticeably absent is the swirling jet-like flow toward the top. Instead, the flow field shows numerous structures that swirl and twist creating vortical structures, nearly of the same size. One region to the right shows a higher velocity magnitude of ~55 m/s indicated by the orange color. Compared to the results from runs with altitude-dependent pressure boundary conditions obtained from the standard atmosphere, this case shows streamlines that are mostly confined to the computational domain (gray cylinder that encloses the streamlines in Fig. 22) without significant inflow and outflow from the side and top boundaries. Thus, this comparison shows the importance of selecting the appropriate boundary conditions in the simulations.

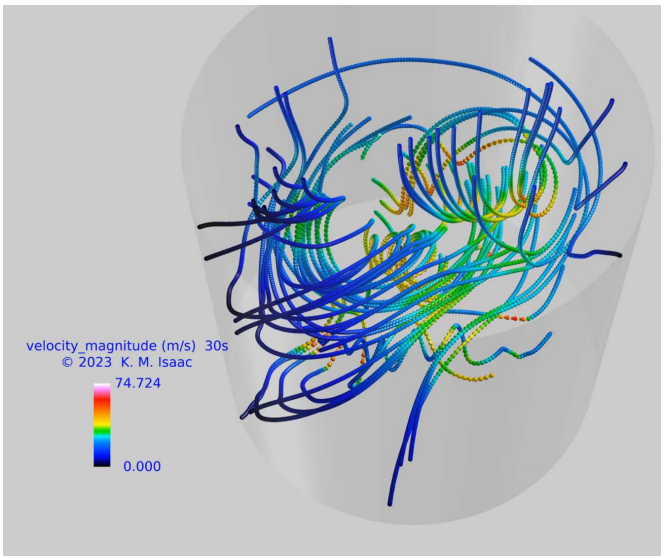

Figure 22. Streamlines from run with constant pressure side and top boundary conditions. t = 30s. Animation file name: *case09_streamlines_30s* (Isaac, 2023)

3.3.8 Translation

From the presented figures it can be observed that the vortex that initially forms at the center of the computational domain translates and undergoes shape distortion with increasing time from the start. Previous studies do not have a consensus whether a tornado can translate in the absence of a superimposed straight-line wind. The present simulations do show that the vortex does translate. The speeds calculated from the simulations fall in the range 2 m/s – 4 m/s. Also to note is that the translation is not along a straight line, but the locations of the axis in the horizontal planes vs. time take irregular paths which depend on the heights from the ground. As a result, the vortex axis does not remain straight, but gets twisted and the vortex breaks up into different segments, each with its own unique characteristics.

3.3.9 Effect of Temperature Variation with Altitude

The atmosphere under ideal conditions with no disturbances present to induce motion will be in a state of unstable equilibrium where the force due to the hydrostatic pressure variation exactly balances the buoyancy force due to density variation. However, in reality, the atmosphere is in an ever-present state of motion due to conditions that are far from those of the model atmosphere. As is well-established, temperature variation is a strong contributing factor that causes powerful wind patterns. To understand the effect of temperature variations that can introduce additional buoyancy force, a few simulations have been run with the Boussinesq model to calculate the buoyancy force. These runs included temperature drops up to 10K between the ground and the top boundary. The results (not included here) show that temperature differences of 10K or less do not have a significant effect on the results. A simulation case was also run with the ground held at a temperature 10K higher to simulate a heated surface. Such a condition could arise due to abnormal atmospheric conditions that can cause rapid cooling of the air above the ground. This case also did not indicate any significant differences in the results from the baseline.

4. Conclusions

This work has investigated a plausible instability mechanism that can trigger the formation of tornados. It is similar to the origin of turbulence discussed by Tennekes and Lumley (Tennekes & Lumley, 1972). A tornado forms by a primary instability mechanism, which in simple cases is two-dimensional. The primary instability introduces secondary motions, which are generally three-dimensional and become unstable themselves. In contrast to transition to turbulence on a flat surface with zero pressure gradient, where random turbulent spots appear as a precursor, the instability mechanism in this work is the rather large two-dimensional Burgers-Rott vortex which stretches and becomes three-dimensional under the influence of the shear present in the ground boundary layer, the vertical pressure gradient, and the buoyance force due to the vertical temperature gradient. The three-dimensional vortex thus formed undergoes different stages in its life span, initially having a well-defined geometric structure, which then enters a phase with large amplitude distortions in the 3D space that is time-dependent, and then breaks up into multiple vortices which are random in size and orientation. This is followed by a decay phase in which the vortices become less distinguishable.

It would be reasonable to expect the nature of the initial instability mechanism to have a significant influence on the subsequent development of the vortical flow field, highlighting the sensitivity to initial conditions. To gain greater insight into tornado life cycle, this research needs to be extended by introducing different types of instabilities, and the corresponding results analyzed. The LES/DES turbulence model and a RANS model such as the SST-kω model or Spalart-Allmaras model for subgrid scale model appear to give satisfactory results, though more powerful turbulence models such as LES that doesn't rely on a RANS model for the SGS may provide better answers, when computers that are powerful enough to handle the mesh size necessary to resolve scales down to the Kolmogorov scale. Such a mesh will be larger by several orders of magnitude than the mesh sizes used in the present simulations. Most of the turbulence models used in tornado simulations have been validated only for Reynolds numbers ~10^6 or less.

They need additional validation for larger Reynolds numbers representative of natural tornados. Validation using data from field measurements of tornado events will further increase the confidence level in the turbulence models.

Further study of the effect large, abnormal temperature patterns that'd introduce large buoyancy forces will provide better understanding of tornados. It'd also help understand the Mars environment with large swings in the temperature and the frequent sitings of dust devils which are believed have the same underlying mechanisms as tornados. Presently there is great interest in studying the Mars environment in light of the planned Mars mission.

Acknowledgements

This work was supported by the NASA Missouri Space Grant Consortium [grant numbers 80NSSC20M0100, NNX15AK03H].

The authors acknowledge discussions with Grace Yan, Hangping Yuan, Yi Zhao, Jiamin Dang, Andrew LeBeau and Leigh Orf.

References

Ansys, Inc., 2022. *Fluent User's Guide,* s.l.: Ansys, Inc..

Bose, S. & Park, G., 2018. Wall-Modeled Large-Eddy Simulation for Complex Turbulent Flows. In: *Annual Review of Fluid Mechanics.* s.l.:Annual Reviews, pp. 1-36.

Bryan, G. & Fritsch, J., 2002. A benchmark simulation for moist nonhydrostatic. *Monthly Weather Review,* Volume 130, pp. 2917-2928.

Cardno, C., 2022. *Civil Engineering Magazine.* [Online]
Available at: https://www.asce.org/publications-and-news/civil-engineering-source/civil-engineering-magazine/issues/magazine-issue/article/2022/10/largest-us-translating-tornado-simulator-opens
[Accessed 27 December 2022].

Davies-Jones, R., 2015. A review of supercell and tornado dynamics. *Atmospheric Research,* Volume 158-159, pp. 274-291.

Davies-Jones, R. & Brooks, H., 1993. Mesocyclogenesis from a Theoretical Perspective. In: *The Tornado: Its Structure, Dynamics, Prediction and Hazards: Geophys. Monogr. No. 79.* s.l.:Amer. Geophys. Union , pp. 105-114.

Davies-Jones, R., Trapp, J. & Bluestein, H., 2001. Tornadoes and tornadic storms. In: *Meteorlogical Monographs.* s.l.:s.n., pp. 28, 50, 167-221.

Frölich, J. & Rodi, W., 2002. Introduction to Large Eddy Simulation of Turbulent Flows. In: B. Launder & N. Sandham, eds. *Closure Strategies for Turbulent and Transitional Flows.* London: Cambridge University Press, pp. 267-298.

Gillmeier, S., Sterling, M., Hemida, H. & Baker, C., 2018. A reflection on analytical tornado-like vortex flow field models. *Journal of Wind Engineering and Industrial Aerodynamics,* 174(March), pp. 10-27.

Isaac, K., 2023. *Missouri S&T Scholars' Mine.* [Online]
https://scholarsmine.mst.edu/mec_aereng_facwork/4889/
[Accessed Monday, 06 February 2023].

Ishihara, T. & Liu, Z., 2014. Numerical study on dynamics of a tornado-like vortex with. *Wind and Structures,* 19(1), pp. 1-23.

Kolmogorov, A., 1941. Dissipation of Energy in Locally Isotropic Turbulence. *Dokl. Acad. Nauk SSSR,* 32(19-21).

Kuai, L., Haan, F., Gallus, W. & Sircar, P., 2008. CFD simulations of the flow field of a laboratory-simulated tornado for parameter sensitivity studies and comparison with field measurements. *Wind and Structures,* II(2), pp. 1-22.

Lewellen, D. & Lewellen, W., 2007. Near-Surface Vortex Intensification through Corner Flow Collapse. *Journal of the Atmospheric Sciences,* 64(7), pp. 2195-2209.

Lewellen, D., Lewellen, W. & Xia, J., 2000. The Influence of a Local Swirl Ratio on Tornado Intensification near the Surface. *Journal of the Atmospheric Sciences,* 57(4), pp. 527-544.

Lewellen, W., 1976. Theoretical models of the tornado vortex. In: *Symp. on Tornadoes: Assessment of Knowledge and Implications for Man.* Lubbock, TX: s.n., pp. 107-143.

Lewellen, W., 1993. Tornado Vortex Theory. In: C. Church, ed. *The Tornado: Its Structure, Dynamics, Prediction, and Hazzards.* Washington D. C.: Geophysical Monograph Service, pp. 19-39.

Lewellen, W., Lewellen, D. & Sykes, R., 1997. Large-Eddy Simulation of a Tornado's Interaction with the Surface. *Journal of the Atmospheric Sciences,* 54(5), pp. 581-605.

Natarajan, D. & Hangan, H., 2012. Large eddy simulations of translation and surface roughness effects on tornado-like vortices. *Journal of Wind Engineering and Industrial Aerodynamics,* Volume 104-106, pp. 577-584.

Piomelli, U. & Balaras, E., 2002. Wall-layer models for large-eddy simulations. Annu. Rev. Fluid Mech. 34:349–74. In: *Annual Review of Fluid Mechanics.* s.l.:Annual Reviews, pp. 181-201.

Pope, S., 2000. *Turbulent Flows.* 1st ed. London: Cambridge University Press.

Refan, M. & Hangan, H., 2016. Characterization of tornado-like flow fields in a new model scale wind testing chamber. *Journal of Wind Engineering and Industrial Aerodynamics,* Volume 151, pp. 107-121.

Reiss, D., Zimmerman, M. & Lewellen, D., 2013. Formation of cycloidal dust devil tracks by redeposition of coarse sands in southern Peru: Implications for Mars. *Earth and Planetary Sciene Letters,* 383(December), pp. 7-15.

Rott, N., 1958. On the Viscous Core of a Line Vortex. *Z. Agnew. Math. Physik,,* Volume 96, pp. 543-553.

Rott, N. & Lewellen, W., 1966. Boundary layers in rotating flows. In: H. Gortler, ed. *Applied Mechanics.* Berlin: Springer, pp. 1030-1036.

Shi, X., Chow, F., Street, R. & Bryan, G., 2018. An Evaluation of LES Turbulence Models for Scalar Mixing in the. *Journal of the Atmospheric Sciences,* 75(5), pp. 1499-1507.

Shur, M., Spalart, P., Strelets, M. & Travin, A., 2008. A hybrid RANS-LES approach with delayed-DES and wall-modelled LES capabilities. *International Journal of Heat and Fluid Flow,* 29(6), pp. 1638-1649.

Spalart, P., 2009. Detached-Eddy Simulation. In: *Annual Rev. Fluid Mech.* . s.l.:annualreviews.org, pp. 181-202.

Spalart, P. & Garbaruk, A., 2020. Correction to the Spalart–Allmaras Turbulence Model. *AIAA Journal,* 58(5), pp. 1903-1905.

Tang, Z. et al., 2018. Characteristics of Tornado-Like Vortices Simulated in a Large-Scale Ward-Type Simulator. *Boundary-Layer Meteorology,* 166(February), pp. 327-350.

Tennekes, H. & Lumley, J., 1972. *A First Course in Turbulence.* 1st ed. Cambridge, MA: MIT Press.

Trapp, J. & Davies-Jones, R., 1997. Tornado Genesis with and Without Dynamic Pipe Effect. *American Meteorological Society,* Volume 54, pp. 113-133.

Verma, S. & Selvam, P., 2020. CFD to VorTECH Pressure-Field Comparison and. *Journal of Structural Engineering,* 146(9), pp. 1-12.

Ward, N. B., 1972. The Exploration of Certain Features of Tornado Dynamics using a Laboratory Model. *Journal of the Atmospheric Sciences,* pp. 1194-1204.

Wurman, J. & Alexander, C., 2005. The 30 May 1998 Spencer, South Dakota, Storm. Part II: Comparison of Observed. *American Meteorological Society,* pp. 97-133.

Yuan, F. et al., 2019. Numerical simulation of laboratory tornado simulator that can produce translating tornado-like wind flow. *Journal of Wind Engineering and Industrial Aerodynamics,* Volume 190, pp. 200-217.

Zuo, D. et al., 2021. Narrowband components in two-celled tornado-like vortices generated in a Ward-type simulator. *Journal of Wind Engineering and Industrial Aerodynamics,* 218(November).